J Therm Spray Tech (2022) 31:2537–2559
https://doi.org/10.1007/s11666-022-01455-4

PEER REVIEWED

Engineered Aluminum Powder Microstructure and Mechanical Properties by Heat Treatment for Optimized Cold Spray Deposition of High-Strength Coatings

Denny John[1] · Tanaji Paul[1] · Kazue Orikasa[1] · Cheng Zhang[1] · Benjamin Boesl[1] · Arvind Agarwal[1]

Submitted: 3 April 2022 / in revised form: 3 August 2022 / Accepted: 4 August 2022 / Published online: 8 September 2022

Abstract The lack of a comprehensive understanding of the role of heat treatments on microstructure and multiscale mechanical properties of powders and their interrelatedness with cold spray process parameters severely impedes the manufacturing of high-strength aluminum coatings. For the first time, this study develops customized heat treatment protocols for controlling microstructure homogenization and intermetallic precipitation in Al 6061 and Al 7075 powders for cold spray. Solution treatment at 505-545 °C, followed by precipitation hardening at 130-160 °C, enables controlled precipitation of hard intermetallic Mg_2Si and $MgZn_2$ phases in Al 6061 and Al 7075, respectively. Strengthening by these phases enhances powder nanohardness of Al 6061 and Al 7075 from 1.0 and 1.5 to 1.6 and 1.8 GPa, respectively. The cumulative response from multiple grains at the micrometer length scale carries the trend to improve microhardness to 131.2 and 177 HV. These characteristics of the precipitation-hardened powder encompass improvements of 13-60% above their pristine gas-atomized counterparts. Experimentally measured powder hardness was employed as input in a cold spray simulation tool to develop *process maps* for manufacturing high-quality coatings. The optimum temperature for deposition with 75-98% efficiencies was established to be 100-300 °C with helium and 500-600 °C with nitrogen and air. In this process window, the particle velocity and critical velocity range of the powders are 998 to 1237 ms^{-1} and 548 to 858 ms^{-1} for helium and 580 to 663 ms^{-1} and 400 to 594 ms^{-1} for air and nitrogen, respectively.

Keywords aluminum alloys · cold spray · nanoindentation · precipitation hardening · process optimization

Introduction

Cold spray is a solid-state deposition technology for manufacturing high-quality aluminum (Al) alloy coatings. The integrity of the coating with a substrate is achieved by mechanical interlocking and metallurgical bonding (Ref 1) even at low process temperatures of 300-450 °C (Ref 2, 3). It thus avoids undesirable thermally induced phase transformations, solute segregation, and oxidation during deposition. Since in-process phase transformations are insignificant, strength enhancements in cold-sprayed coatings can be achieved only by two approaches. The first approach is to heat-treat the feedstock powder to enhance its strength a priori, while the other involves post-spraying heat treatment of the coating. The latter is challenging since it introduces structural changes in the coated component and may be logistically complicated owing to the large size of coated components. It is thus more important to devise strategies to improve the mechanical properties of the feedstock powder before cold spray by heat treatment.

The typical feedstock Al alloy powder used for cold spray deposition is produced by gas atomization. A liquid metal stream is impinged by a high-velocity inert gas to disintegrate them into fine droplets and solidify them into powder particles. Here, the alloy is subjected to high cooling rates of 10^4 to 10^7 Ks^{-1} (Ref 4). This results in rapid solidification such that solute atoms do not get

✉ Arvind Agarwal
agarwala@fiu.edu

[1] Plasma Forming Laboratory, Department of Mechanical and Materials Engineering, Florida International University, 10555 West Flagler Street, Miami, FL 33174, USA

sufficient time to diffuse and dissolve into the crystal lattice. This leads to chemical segregation of the solute atoms on grain boundaries, resulting in a non-homogeneous microstructure and variation in mechanical properties throughout the powder (Ref 5, 6). This chemical segregation is retained in the microstructure of cold-sprayed Al alloy coating due to the solid-state nature of the process (Ref 7). When subjected to stress, these segregations will act as weakening sites, undermining the coating's bulk mechanical properties and strength. Therefore, it is critical to engineer the properties of the feedstock Al alloy powder before cold spray deposition to achieve high strength in the consolidated coating. These challenges in the gas-atomized powder can be addressed by tailoring the powder's microstructure using heat-treatment strategies.

The primary heat treatments that can be performed on Al alloy powder to modify the microstructure are grouped into solution treatment and precipitation hardening or aging. A few experimental studies have employed solution treatment on F 357, Al-Cu, Al 2024, Al 5056, Al 6061, and Al 7075 powder (Ref 8-22). In addition, one study has utilized precipitation hardening on Al 7075 powder [9]. These showed that solution-treated powder with a low hardness of around 60 to 80 HV is not suitable for developing high-strength coating [9]. However, it can prepare segregation-free powder for subsequent precipitation hardening. Precipitation-hardened Al 7075 powder showed 117% and 40% improved cohesion strength and hardness, respectively, in the final coating compared to that deposited using a solution-treated one. But this study is limited to only one precipitation hardening condition [9]. However, Al alloys show time-temperature-dependent property variation or aging. *Hence performing an investigation in one aging temperature and time does not provide a comprehensive understanding of the overall aging behavior of Al alloy powders.* Moreover, the previous experimental studies do not provide an understanding of the multiscale mechanics of the heat-treated powder. Due to the solid-state nature and hierarchical microstructure of the cold spray process, the performance of the coating strongly depends on the mechanics of the heat-treated powder. This mandates unraveling the mechanical properties and underlying strengthening phenomena in heat-treated Al alloy powder at systematically progressive length scales.

Another factor to consider for successful cold spray coating development using Al alloy powder aged at multiple durations is the optimization of parameters to develop a process map (Ref 23-26). However, depositing powders aged at multiple aging times requires extensive experiments, which is time-consuming and cost-prohibitive. This challenge can be addressed by simulation techniques designed for the cold spray process to establish boundaries of process parameters for manufacturing high-quality coatings with heat-treated Al alloy powder (Ref 23-26).

In summary, the absence of a comprehensive understanding of the correlations between microstructure engineering in Al powder, their multiscale mechanical properties, and cold spray process parameters severely impedes the development of high-strength coatings. The present investigation aims to establish a fundamental understanding of the role of heat treatment strategies on the evolution of precipitate phases in gas-atomized Al alloy powder. The strengthening effect of these precipitates is probed from individual grains to entire powder particles from nano- to micro-meter length scales. These feedstock properties are input in a cold spray simulation tool to develop process maps for manufacturing high-quality Al alloy coatings. For utility in commercial applications, this study focuses on investigations on Al 1100, Al 6061, and Al 7075. Al 1100 is selected as a reference since it is a pure composition without any solute atom segregation. On the other hand, Al 6061 and Al 7075 powders are widely employed medium- and high-strength powders for cold spray deposition.

Materials and Methods

Aluminum Alloy Powder

The feedstock materials used in this investigation were gas-atomized Al alloy powder, namely Al 1100, Al 6061, and Al 7075 (Valimet Inc, USA). The morphology of the powder exhibited a spherical shape, as shown in Fig. 1(a), (b) and (c). They demonstrated a Gaussian distribution with a mean diameter of 22 $\pm$ 11, 52 $\pm$ 18 and 22 $\pm$ 17 μm for Al 1100, Al 6061, and Al 7075 powder, respectively, as depicted in Fig. 1(d), (e) and (f). The composition of the Al 1100, Al 6061, and Al 7075 powder is presented in Table 1. The terminology for gas-atomized, solution-treated, and precipitation-hardened powders will be followed by abbreviations GA, ST, and PH, respectively.

Al Alloy Powder Heat Treatment

Al 1100, a commercially pure composition, was excluded from heat treatment. The gas-atomized Al 6061 and Al 7075 powders were subjected to solution treatment and precipitation hardening. The temperature and treatment time were selected to induce desired microstructural modification while avoiding powder sintering, and melting of Al, and solute atoms such as magnesium, silicon, zinc, and secondary phases. Solution treatment time was kept at 1 h as the literature indicated the growth and coarsening of

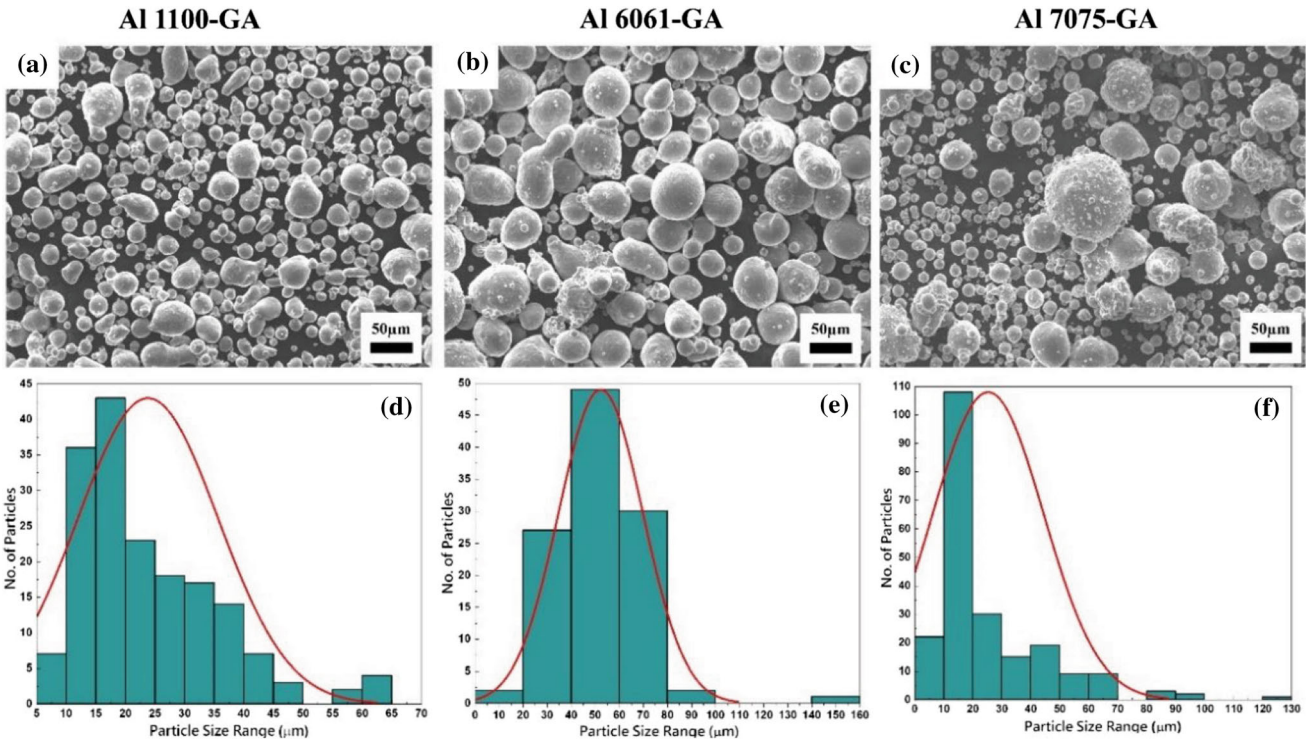

Fig. 1 Morphology and size distribution of the gas-atomized (GA) Al alloy powder. (a) Al 1100-GA, (b) Al 6061-GA, and (c) Al 7075-GA powders consist of primarily spherical particles. The corresponding size of (d) Al 1100-GA, (e) Al 6061-GA, and (f) Al 7075-GA shows a Gaussian distribution with a mean diameter of 22 ± 11 µm, 52 ± 18 µm, and 22 ± 17 µm, respectively

Table 1 Chemical composition (at.%) of gas-atomized (GA) Al 1100, Al 6061 and Al 7075 powder

Al Powder	Alloying elements (at.%)									
	Al	Cr	Cu	Fe	Mg	Mn	Si	Ti	Zn	Other
Al 1100-GA	99.50			0.10						0.40
Al 6061-GA	98.09	0.05	0.12	0.04	1.10	< 0.01	0.58	0.01	< 0.01	0.01
Al 7075-GA	94.20	0.12	0.81	0.06	2.45	< 0.01	0.11	0.02	2.23	0.01

some secondary phases at prolonged times beyond 4 h [19].

The heat treatment of powder is conducted inside a vacuum tube furnace (Lindberg/Blue M, USA). The powder is placed in the tube furnace on a ceramic combustion boat. Argon is purged into the tube furnace, and the gas is extracted using a vacuum pump. Solution treatment of the powder is performed in vacuum. After solution treatment, the powder was quenched in water to ambient temperature to arrest the solute atoms from reprecipitation. After quenching, the powder is separated using a filter paper and dried. Precipitation hardening experiments were conducted on quenched solution-treated powder in the vacuum and cooled to ambient temperature. After cooling, the vacuum is removed, and the powder is subjected to experimental investigations. The temperatures and times of heat treatment are presented in Table 2, and the corresponding phase diagram and the expected microstructural changes are provided in Fig. S1 in the supplementary file.

Al Alloy Powder Specimen Preparation

The gas-atomized and heat-treated Al 1100, Al 6061, and Al 7075 powder were cold-mounted in an epoxy resin. While mounting, the powder was spread to observe and analyze individual particles. They were ground by silicon carbide papers of grit sizes 600 and 1200. Final cloth polishing was performed using 1 µm alumina and 0.05 µm silica suspension to a mirror finish. For observing the microstructure, the samples were etched by Keller's reagent for a time interval of 5 s until the grain boundaries were revealed.

Table 2 Temperatures and times used for heat treatment of gas-atomized (GA) Al 6061 and Al 7075 powder

Heat treatment	Al 6061-GA	Al 7075-GA
Solution treatment	545 °C, 1 h	505 °C, 1 h
Precipitation hardening	545 °C, 1 h and 160 °C, 18 h	505 °C, 1 h and 130 °C, 24 h
Aging	545 °C, 1 h and 160°C, 0 to 24 h	505 °C, 1 h and 130°C, 0 to 48 h

Microstructural Investigations of Al Alloy Powders

The cross-section of the powder specimens was investigated by an optical microscope (OM) (Zeiss, Axio Lab.A1). A scanning electron microscope (SEM) (JEOL, F100) was utilized for acquiring secondary electron (SE) and backscattered electron (BSE) images for studying the microstructure and elemental distribution before and after heat treatment. The compositional variation in the powder cross-section was studied using energy-dispersive spectroscopy (EDS) analysis. The volume of the secondary phases after heat treatment was calculated by an open-source image analysis software, ImageJ (NIH, USA). The area fraction calculated from the ImageJ is assumed to equal the volume fraction of the secondary phases in the gas-atomized powder.

Multiscale Mechanical Response of Al Alloy Powders

The role of heat treatment on the mechanical behavior of gas-atomized and heat-treated Al alloy powder was investigated at systematically progressing length scales using nanoindentation and micro-indentation techniques. Nanoindentation experiments were conducted using a Triboindenter (Bruker, TI900) equipped with a Berkovich tip in load-controlled mode. The experimental parameters for nanoindentation were optimized by conducting a series of experiments with a systematic variation of force from 0.25 to 1.5 mN on the powder mounted in the resin. At low forces such as 0.25 mN, the displacement was comparable to the indenter tip radius of 50 nm. Under these conditions, measured values of hardness and elastic moduli become unreliable.

In contrast, at high forces such as 1.5 mN, the displacement was significantly high such that the volume of plastic deformation manifested contributions from both the powder and underlying resin. Hence in both of these conditions, the inherent mechanical properties of the powder cannot be accurately measured. Therefore, the force was optimized at 1 mN for performing nanoindentation experiments for all powder conditions where the above effects got eliminated. In the loading segment, a peak force of 1 mN was employed for 10 s at a loading rate of 100 μNs^{-1}. This was followed by a dwell time of 5 s, during which the force was maintained constant at 1 mN. Following this, in the unloading segment, the employed force was removed entirely in a duration of 10 s at an unloading rate of 100 μNs^{-1}. Twenty experiments, each on an individual powder particle, were conducted to enumerate the statistical variation in the mechanical response of the powder particles. The force–displacement curve, average nanohardness, and average elastic modulus are reported.

A nano-dynamic mechanical analyzer (nano-DMA) was employed to map elastic modulus distribution on the gas-atomized powder. A static force of 1 μN, a dynamic force of 0.3 μN, and a frequency of 200 Hz were used to achieve an optimal balance between low elastic deformation, high resolution, and low noise. Static forces for nano-DMA are selected to obtain purely elastic deformation in the specimen. These forces range from 1 to 5 μN. In general, lower forces like 1 μN are employed for relatively softer materials such as aluminum. Dynamic forces are usually kept 10-50% of static force to extract a reasonable amplitude of vibration. Too low amplitudes are challenging to detect reliably, while too high amplitudes increase the noise of acquired data. Based on these considerations, a dynamic force of 0.3 μN was employed in this study. The frequency is kept toward the higher end of the instrument capability, at 200 Hz to extract elastic modulus information for the powder that would be related to its deformation during cold spray deposition. The elastic modulus distribution was measured over a square area of 400 μm^2 (20 × 20 μm) on the powder cross-section. The elastic modulus distribution of the powder cross-section is presented as a high-resolution map consisting of (256 × 256 = 65,536) pixels.

Micro indentation was performed on the powder specimens using a Vickers hardness testing machine (Leco Corporation, LM810AT) to probe the mechanical response from a plastic volume at a micrometer length scale. The indentations on the powders were performed using a load of 10 gf or 0.098 N, exactly at the center of the powder particles, to avoid influence from the varying thickness of underlying semispherical powder particles. This load was chosen by performing experiments at different loads ranging from 5 to 25 gf. At loads above 10 gf, the penetration depth and the plastic volume of the indent were high such that it got influenced by both the underlying resin and the powder particle. This is manifested as a distorted diamond indent shape with an abnormal change in the length of the sides of the indent. At a load of 10 gf and less, the penetration depth and plastic volume of the indent are low.

The contribution to hardness is purely from the powder particle alleviating resin effects. This is observed as a uniform indent shape with equal length of the sides of the diamond indent and a comparable hardness response to the literature data of gas-atomized powder. Finally, the load is kept constant at 10 gf, so the bulk hardness response is probed by indenting enough grains, grain boundaries, and precipitates. To evaluate the variation in microhardness over different individual powder particles, at least 20 particles were indented, and the average microhardness value was reported.

Development of Aging Window of Al 6061 and Al 7075 Powder

Artificial aging was conducted on Al 6061 and Al 7075 powder to unravel microhardness evolution with aging time at a constant temperature. The experiments were carried out on solution-treated and quenched powder specimens. The temperature and time used for the aging treatments are presented in Table 2. The aging time interval was selected as 3 h starting from 0 h and increased progressively until the average microhardness value showed a decreasing trend. After the heat treatment, the samples were mounted, polished, and subjected to microhardness evaluation according to the procedures stated in the previous sections. The aging curves' trends of hardness evolution were used to demarcate corresponding windows of deformation behavior in Al 6061 and Al 7075 during cold spray deposition.

Modeling of Process Parameters for Cold Spraying Aged Al Alloy Powders

The KSS software (Kinetic Spray Solutions, Germany) was used to optimize the cold spray process parameters as a function of aging temperature, time, and the corresponding change in average microhardness for engineered aluminum powders. KSS software has been used to determine the optimum process parameters before cold spray deposition (Ref 23-59). The simulation takes into consideration the significant process parameters such as equipment configuration (nozzle geometry), process gas parameter (temperature, pressure, and type), powder (size and mechanical property), and powder feed rate. These process variables converge to generate a set of dependable output characteristics such as optimum velocity ratio and deposition efficiency (Ref 23-26).

The inputs for the present simulation are equipment configuration, powder feeder parameters, process gas parameters, heat-treated powder ultimate tensile strength, and powder size. The equipment configuration CGT K 4000-47 with nozzle dimensions of D51WC and Powder feeder PF 4000 Lochscheibe were selected for performing the simulation. The nozzle D51WC has a pre-chamber radius of 0.007 m, throat radius of 0.00165 m, divergent length of 0.180 m, and expansion ratio of 6.4. The average microhardness value of Al 6061 and Al 7075 at different aging times was converted to ultimate tensile strength using Eq 1 (Ref 60) for the simulation

$$\sigma_{UTS} = 0.189H - 1.38 \quad \text{(Eq 1)}$$

where σ_{UTS} is the ultimate tensile strength (MPa), and H is the Vickers microhardness (MPa). The specific process gas parameters used for simulation are presented in Table 3. The output parameters of the simulation, such as particle velocity, temperature, critical velocity, coating quality factor (velocity ratio), and deposition efficiency, are reported. A cold spray process map is developed for depositing heat-treated Al 6061 and Al 7075 powder using the average microhardness, velocity ratio, and deposition efficiency. Details regarding the principles of calculations used in KSS software are provided in the published literature (Ref 24-26) and in the supplementary information.

Results and Discussion

Microstructure and Elemental Distribution of Gas-Atomized Al Alloy Powders

The microstructure of gas-atomized powders was studied as a reference to understand the microstructural evolution after heat treatment. The optical microstructures of Al 1100, Al 6061, and Al 7075 powders are presented in Fig. 2(a), (b) and (c). They consist of a polycrystalline microstructure with equiaxed grains of 2 to 5 µm. In addition, a few dendritic grains are also observed. This is possibly due to the high cooling rates encountered by the particles during gas atomization (discussed later). BSE images acquired to obtain the solute and secondary phase distribution in the Al 6061 and Al 7075 powder are reported in Fig. 3(a) and (b), and (d) and (e), respectively. The corresponding investigation was not conducted for Al 1100 since it does not have significant alloying elements. BSE images show a contrast difference in the

Table 3 Cold spray parameters employed in simulation for developing process maps

Process gas parameters	Input values for simulation
Carrier gas	Nitrogen, Helium
Gas pressure (MPa)	2, 4
Gas temperature (°C)	100 to 600

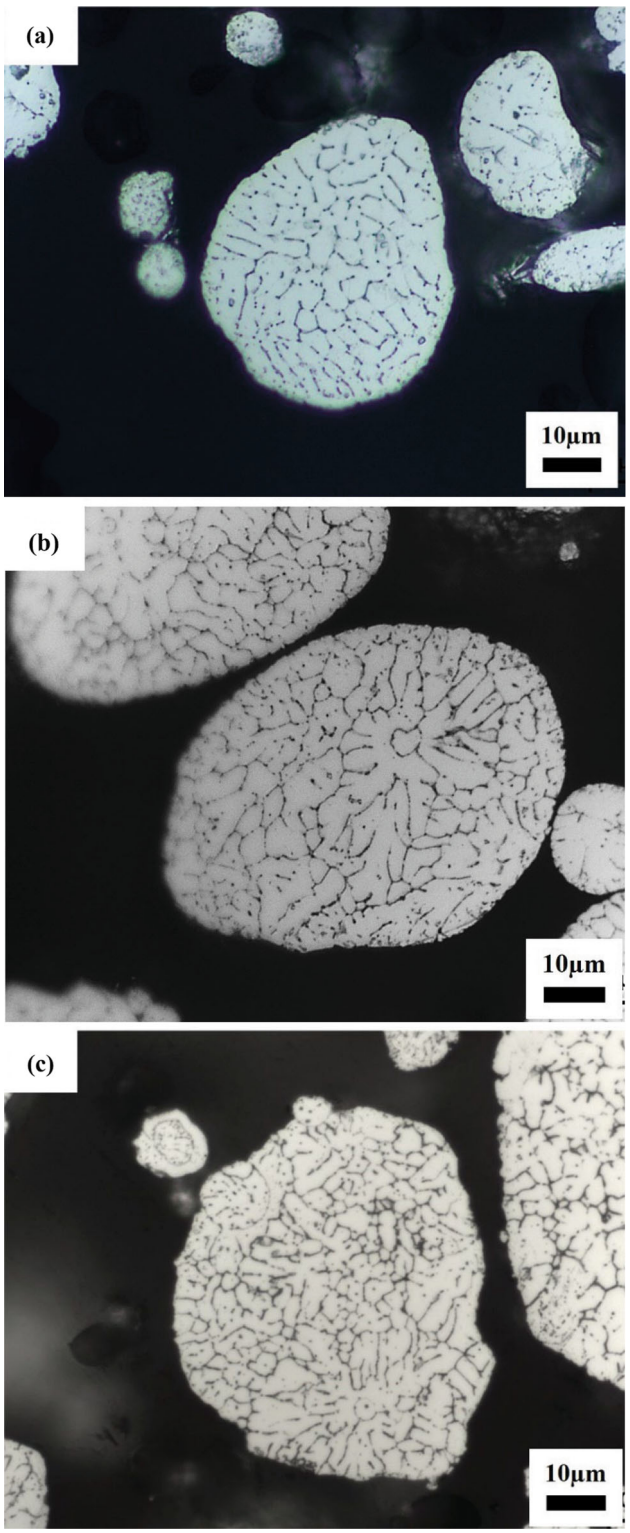

Fig. 2 Optical micrographs of the cross-sections of gas-atomized (GA) (a) Al 1100-GA, (b) Al 6061-GA, and (c) Al 7075-GA powder. All the gas-atomized micrographs exhibited polycrystalline equiaxed grains of diameter around 2 to 5 µm

microstructure according to the element's atomic number (Z). Herein, the major element is aluminum with atomic number (Al, $Z = 13$) compared to the alloying elements such as magnesium (Mg, $Z = 12$), silicon (Si, $Z = 14$), zinc (Zn, $Z = 30$), iron (Fe, $Z = 26$). The BSE microstructure shows gray-, white-, and black-colored regions according to the contrast difference. The gray-colored regions correspond to Al. The white-colored regions correspond to heavier atoms or secondary phases, dominated by Si, Zn, and Fe. The black regions correspond to Mg or Mg-rich secondary phases. Therefore, from these micrographs, it can be concluded that undissolved solute or secondary phases are heterogeneously segregated across the grain boundaries compared to the grain interior. The volume of the segregated phase in the microstructure of Al 7075 powder (Fig. 3e) was visibly higher than that in Al 6061 powder (Fig. 3b).

Elemental distribution on the grain and grain boundaries of the Al alloy powder was delineated by EDS maps as presented in Fig. 3(c) and (f). In Al 6061, most magnesium, silicon, copper, and iron are segregated at grain boundaries with relatively lesser amounts inside the grain, as depicted in Fig. 3(c). Similarly, in Al 7075, most magnesium, zinc, iron, copper, and silicon are observed across the grain boundaries with relatively lesser amounts inside the grain, as shown in Fig. 3(f). From EDS-point scans performed inside the grains and at grain boundaries and presented in Table 4, it is concluded that the volume of chemical segregation is more significant at the grain boundaries than at the grain interior. Hence, the point scans confirm and validate the EDS map observations.

The gas atomization process has a high cooling rate, at 10^4–10^7 Ks^{-1} (Ref 4). Higher rates lead to faster solidification, and the solute atoms do not get sufficient time to diffuse into the crystal lattice. As a result, these solute atoms are segregated across the grain boundaries as undesirable secondary phases that undermine the powder's mechanical properties (Ref 5, 6). They act as crack initiation sites under applied stress and can reduce the ductility leading to catastrophic failure of the coating. Hence, from the microstructural and EDS observations, solute heterogeneity in the powder must be circumvented by heat treatment.

Effect of Heat Treatment on Microstructure of Gas-Atomized Al Alloy Powder

The gas-atomized Al 6061 and Al 7075 powders were subjected to solution and precipitation hardening heat treatment as described in Table 2. BSE microstructures of

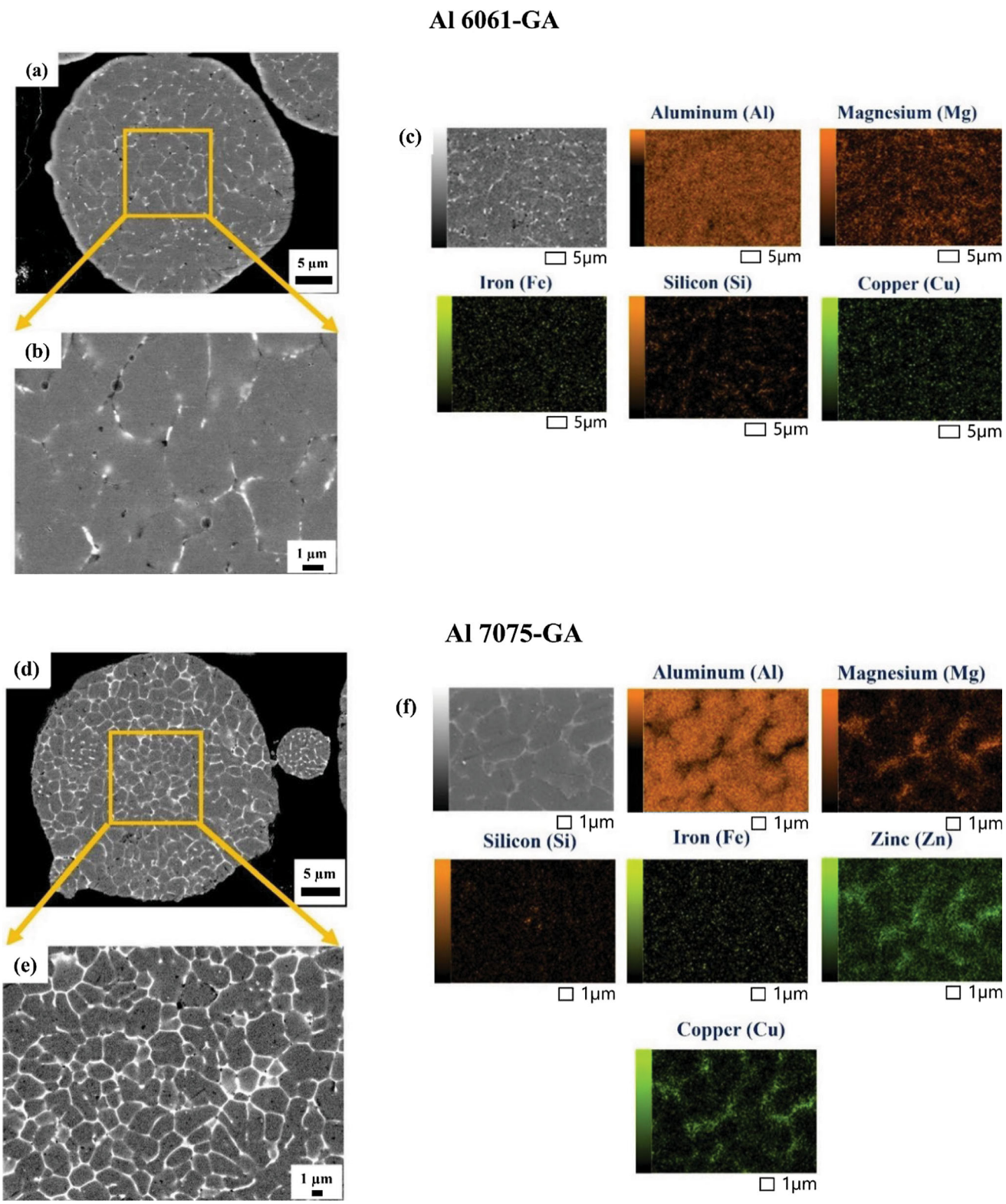

Fig. 3 BSE micrographs of gas-atomized (GA) Al alloy powders in low and high magnifications (a & b) Al 6061-GA and (d & e) Al 7075-GA. The white and black regions in the microstructure indicate the heterogeneously segregated solute atoms or secondary phases. EDS elemental distribution on the cross-section of (c) Al 6061-GA and (f) Al 7075-GA powder shows that elements like Mg, Zn, Si, and Cu are present primarily at the grain boundaries

Table 4 Distribution of elements (at.%) across the grain interior and grain boundary of gas atomized (GA) Al 6061 and Al 7075 powder.

Elements	Al 6061-GA		Al 7075-GA	
	Grain Interior	Grain Boundary	Grain Interior	Grain Boundary
Aluminum (Al)	98.75 ± 10.00	96.88 ± 0.10	89.62 ± 0.09	77.79 ± 0.08
Magnesium (Mg)	0.48 ± 0.01	**0.87 ± 0.01**	3.32 ± 0.02	**9.01 ± 0.03**
Silicon (Si)	0.17 ± 0.02	**0.97 ± 0.02**	0.49 ± 0.01	0.45 ± 0.01
Iron (Fe)	0.00	0.08 ± 0.01	0.42 ± 0.03	0.35 ± 0.03
Copper (Cu)	0.00	0.41 ± 0.02	1.72 ± 0.01	**4.29 ± 0.02**
Zinc (Zn)	…	…	2.93 ± 0.01	**6.67 ± 0.02**

Values in bold show the significant concentration of solute atoms at the grain boundary compared to grain interior

treated Al 6061 and Al 7075 are presented in Fig. 4(c), (d), (e) and (f), and (i), (j), (k) and (l). The solution-treated powder microstructure of Al 6061 (Fig. 4c and d) and Al 7075 (Fig. 4i and j) indicates the dissolution of the segregated secondary phase network from the grain boundaries. This is manifested as a lower volume fraction of white- and black-colored segregated regions in the microstructure than in gas-atomized Al 6061 and Al 7075 powder presented in Fig. 4(a) and (b), and (g) and (h), respectively. ImageJ software analyzed multiple images of gas-atomized and solution-treated Al 6061 and Al 7075. Solution treatment dissolved 87% and 92% of the heterogeneously segregated secondary phases in Al 6061 and Al 7075, respectively. The microstructures of precipitation-hardened Al 6061 (Fig. 4e and f) and Al 7075 (Fig. 4k and l) show the formation of small precipitates (white-colored) at the grain interiors.

Solution treatment in Al alloys is generally performed at a temperature above the solvus line. In the present investigation, this procedure was conducted at a temperature of 545 and 505 °C for Al 6061 and Al 7075 powder, respectively, above the solvus lines of the respective phase diagrams as presented in the supplementary file, Fig. S1 (Ref 61, 62). At these temperatures, the alloyed solute atoms such as Mg, Si, and Zn have sufficient activation energy to diffuse into the Al lattice to form a complete solid solution (Ref 63). Due to rapid water quenching, these dissolved solute atoms are arrested inside the crystal lattice and restricted from reprecipitation. This restriction of the solute atoms is observed as the reduction in the volume fraction of segregated phases in the microstructure of Al 6061 (Fig. 4c and d) and Al 7075 (Fig. 4i and j) powder. Hence, solution treatment enables homogenizing the non-uniform microstructure of the gas-atomized Al powder.

On the other hand, precipitation hardening of Al alloys is generally conducted below the solvus line at a range of temperatures from ambient to 300 °C. However, at such high temperatures, the growth kinetics of the precipitates are high, resulting in coarsening. Thus, in the present investigation, precipitation hardening of Al 6061 and Al 7075 was conducted at 160 and 130 °C. At these lower temperatures, the solubility of Mg, Si, and Zn atoms in the Al crystal lattice is low. Therefore, these atoms gradually precipitate and form hard intermetallic phases such as Mg_2Si, and $MgZn_2$.

The BSE micrographs of solution-treated and precipitation-hardened powder indicated white and black regions of contrast as presented in Fig. 4(c), (d), (e), (f), (i), (j), (k) and (l). This contrast is obtained from the secondary phases due to the difference in the atomic number of the elements. Multiple EDS maps and point scans were acquired to understand the elemental distribution from these regions. These EDS maps and point scans are provided in the supplementary file (Fig. S2 to S4). In Al 6061 microstructure, the phases with black contrast are rich in Mg and Si, whereas those with white contrast are rich in Fe (Fig. 4d and f). These phases of black contrast have been identified as Mg_2Si, and white contrast ones as $Al_9Fe_2Si_2$ in the literature during solution treatment of Al 6061 powder at 530 °C by a combination of SEM, TEM, and Thermo Calc calculations (Ref 19, 22). In the corresponding regions of black and white contrast in Al 7075 microstructure (Fig. 4j and l), EDS scans showed that black phases are rich in Mg and Si, while white contrast areas are grouped into regions rich in Cu and Fe and regions rich in Mg and Zn. From the literature, these phases of black contrast have been identified as Mg_2Si, and the white contrast region rich in Cu and Fe to be Al_7Cu_2Fe during solution treatment of Al 7075 at 450 to 480 °C (Ref 8, 15). The white phase rich in Mg and Zn is $MgZn_2$, the main strengthening precipitate of Al 7075.

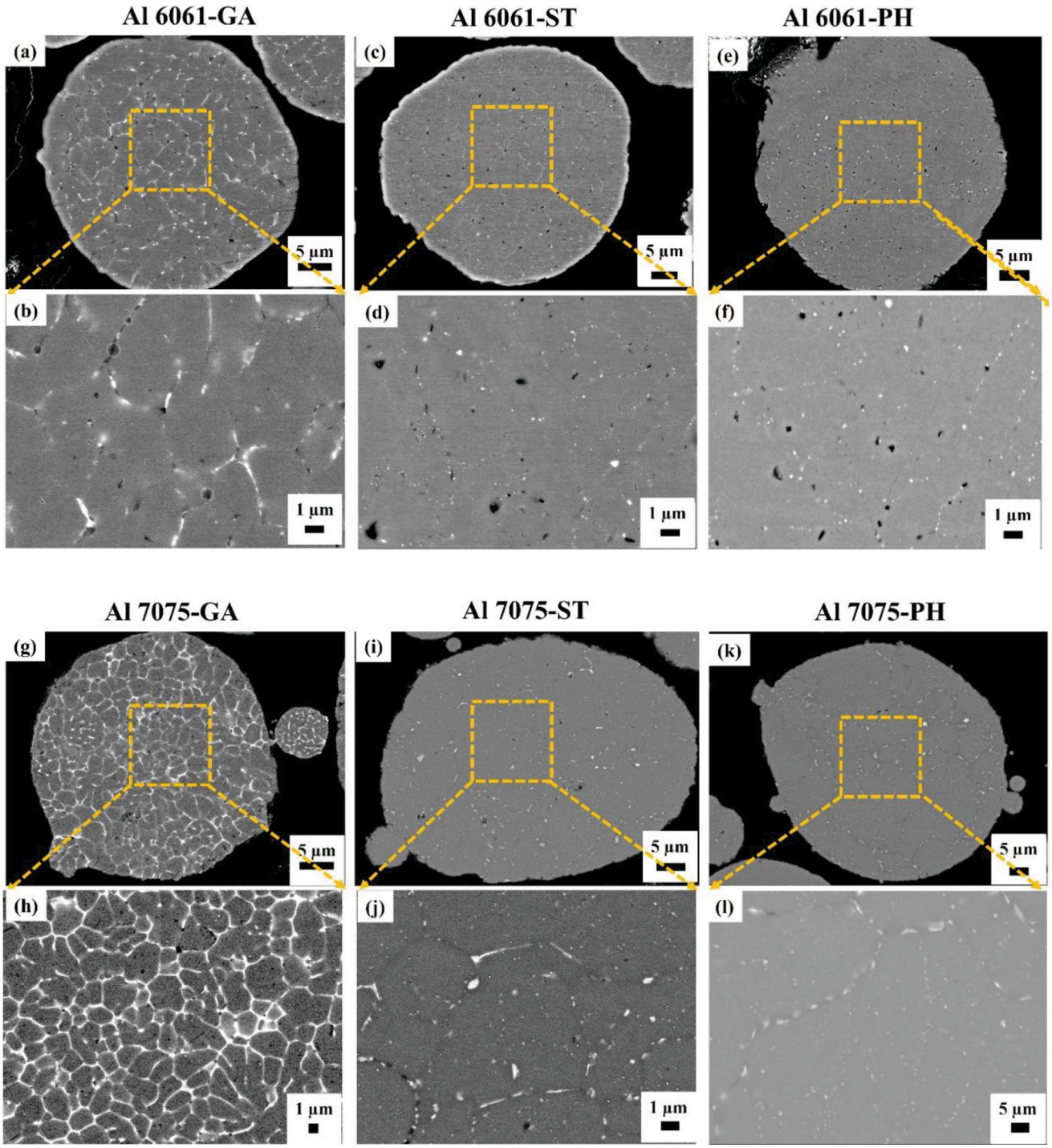

Fig. 4 BSE micrographs of the gas-atomized (GA), solution-treated (ST), and precipitation-hardened (PH) Al alloy powders in low and high magnifications, (a and b) Al 6061-GA (c and d) 6061-ST (e and f) Al 6061-PH (g and h) Al 7075-GA (i and j) Al 7075-ST and (k and l) Al 7075-PH. The microstructures show that the volume fraction of segregated secondary phases in the gas-atomized powder is minimized in the solution-treated powder. Further precipitation hardening leads to the formation of fine precipitates in the powder

Multiscale Hardness and Elastic Modulus of Gas-Atomized and Heat-Treated Al Alloy Powder

The hardness of the powder at the individual grain and particle length scales provides insights into plastic deformation at the core and entirety of splats during cold spray deposition. On the other hand, elastic modulus controls the extent of localized elastic deformation and localized strain in the interior and periphery of the powder. This rate of plastic deformation will influence the extent of

dynamic recrystallization at the intersplat jetting regions and the overall bulk elastic deformation of the coating. Hence, this section focuses on understanding the role of microstructural homogenization and controlled precipitation on the nano- and microscopic hardness and elastic modulus of the Al alloy powder at the grain and particle levels, respectively.

Nanohardness Response of Gas-Atomized and Heat-Treated Al Alloy Powders

This section evaluates the change in nanohardness at a single grain level as a function of heat treatment. This was delineated by conducting nanoindentation investigations on Al 1100, Al 6061, and Al 7075 powder in gas-atomized, solution-treated, and precipitation-hardened conditions; the representative force–displacement plots are obtained during the applied compressive force. Figure 5(a) presents the representative force-displacement plots obtained during the applied compressive force on Al 1100, Al 6061, and Al 7075 powder cross-sections. The loading and unloading plots of the gas-atomized and the heat-treated Al powders do not overlap, indicating the change in the resistance toward the applied compressive force after heat treatment. After elastic recovery, the gas-atomized Al 1100 exhibited the highest penetration depth of 179 nm. For Al 6061, the penetration depth progressively reduced from gas-atomized, solution-treated to precipitation-hardened from 147, 128 to 111 nm, respectively. Similarly, for Al 7075, the corresponding depths are 117, 110, and 96 nm. Therefore, the penetration depth decreased progressively from gas-atomized to solution-treated to precipitation-hardened Al 6061 and Al 7075 powder. Thus, it can be concluded that heat treatment enhanced the nanoscale resistance of the gas-atomized powder.

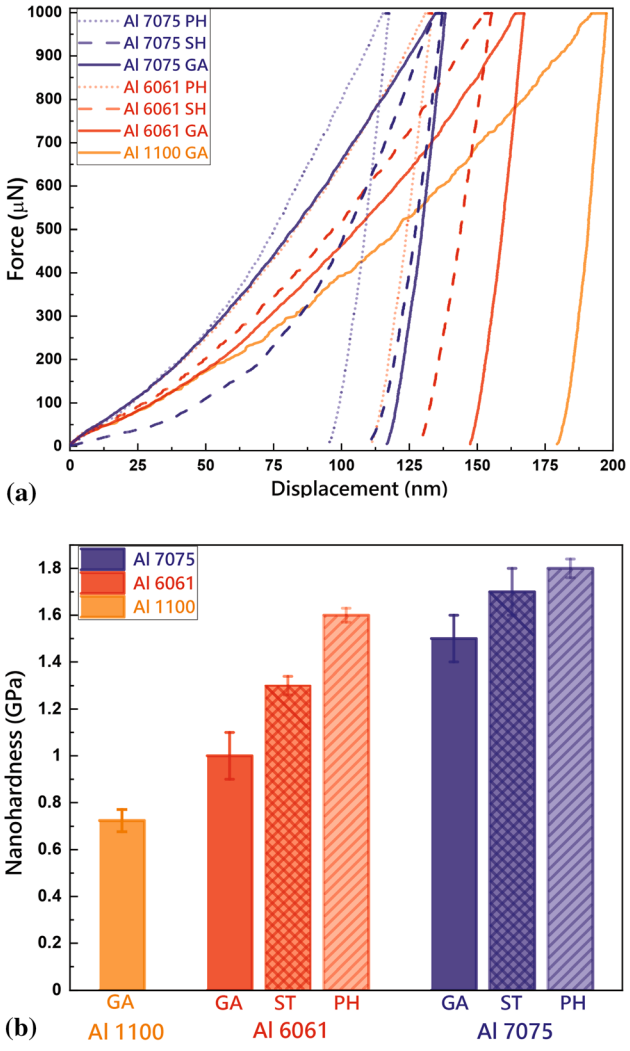

Fig. 5 (a) Representative force–displacement response and (b) average nanohardness of Al 1100, Al 6061, and Al 7075 powder in the gas-atomized (GA), solution-treated (ST), and precipitation-hardened (PH) conditions. The average nanohardness is highest for precipitation-hardened powder, followed by solution-treated and gas-atomized counterparts

The average nanohardness of Al 1100, Al 6061, and Al 7075 at different processed conditions is presented in Fig. 5(b). Gas-atomized Al 1100, a commercially pure Al alloy devoid of solute atoms, showed the lowest average nanohardness at constant force compared to the alloyed powders. In Al 6061 and Al 7075 powder, the average nanohardness increased progressively from gas-atomized, solution-treated to precipitation-hardened powders. The average nanohardness of gas-atomized Al 6061 powder is measured as 1.00 ± 0.10 GPa. However, solution treated and precipitation-hardened Al 6061 powder resulted in a 30% and 60% increase to 1.30 ± 0.04 and 1.60 ± 0.03 GPa, respectively. The average nanohardness of gas-atomized Al 7075 powder is 1.50 ± 0.10 GPa. Solution treatment and precipitation hardening resulted in a 13% and 20% increase to 1.70 ± 0.10 and 1.80 ± 0.04 GPa, respectively.

During nanoindentation experiments, the compressive deformation of the powder occurs at a nanometer length scale. As discussed earlier, rapidly solidified gas-atomized Al 6061 (Fig. 3a) and Al 7075 (Fig. 3d) powders contain heterogeneously segregated solute atoms or secondary phases along the grain boundaries. Therefore, the grain interior lacks solute atoms that contribute to hardening. Thus, gas-atomized powders lack resistance to deformation when a force is applied at a nanometer length scale, manifested as the lowest average nanohardness in all Al alloy compositions. Solution-treated Al alloy powder showed higher average nanohardness than gas-atomized powder. During solution treatment at elevated temperature (545 °C for Al 6061 powder and 505 °C for Al 7075 powder), the solubility of the solute atoms is high such that diffusion occurs into the Al crystal lattice to attain

equilibrium. The atomic radius of the solute atoms differs from that of the Al atoms, which creates a lattice misfit. For example, the atomic radii of the primary atoms in Al 6061 alloy are Al with an atomic radius of 0.143 nm, Mg with 0.160 nm, and Si with 0.132 nm. Mg causes + 13%, and Si causes − 8% misfit in the Al crystal lattice (Ref 63). This misfit leads to lattice distortion caused by localized tensile and compressive strains around the larger Mg and smaller Si atoms. These localized strains restrict dislocation motion inside the Al crystal. During nanoindentation, applied to a nanometer length scale (90-175 nm), force is influenced by these solid solution strengthening effects, causing the alloy's average nanohardness to increase compared to the gas-atomized counterparts. Precipitation-hardened Al alloy powders showed the highest average nanohardness compared to the solution-treated and gas-atomized powders. It is caused by the uniform distribution of hard intermetallic phases precipitated within the Al alloy matrix, such as Mg_2Si in Al 6061 and $MgZn_2$ in Al 7075 powder. These hard precipitates resist the dislocation movement, increasing the average nanohardness in precipitation-hardened powders to the highest among all powder conditions.

The nanohardness of the powder dictates the extent of plastic deformation during the cold spray deposition. The deformation response at the nanoscale controls the mechanical interlocking and metallurgical bonding of the powder with the substrate and prior splats during cold spray deposition. The coating interface with the substrate and the intersplat bonding control the bulk coating integrity. Hence, it can be understood that the nanoscale mechanical characteristics play a significant role in the bulk coating performance.

Microhardness Behavior of Gas-Atomized and Heat-Treated Al Alloy Powders

Due to the solid-state nature of cold spray deposition, powder properties are directly translated during cold spray to the bulk coating, thus necessitating an understanding of the hardness of the powder. Hence, in addition to the localized response obtained from nanomechanical studies, microhardness investigations were conducted on the gas-atomized and heat-treated powder to understand the cumulative resistance of multiple grains and grain boundaries to plastic deformation. Figure 6 presents the average microhardness of Al 1100, Al 6061, and Al 7075 in different heat treatment conditions. Gas-atomized Al 1100 showed a low average microhardness of 31.40 ± 1.70 HV. This hardness is comparable to the microhardness of wrought Al 1100, which is 32 HV. The average microhardness of gas-atomized Al 6061 is 95.0 ± 4.6 HV. The solution-treated Al 6061 showed a 26.8% decrease to

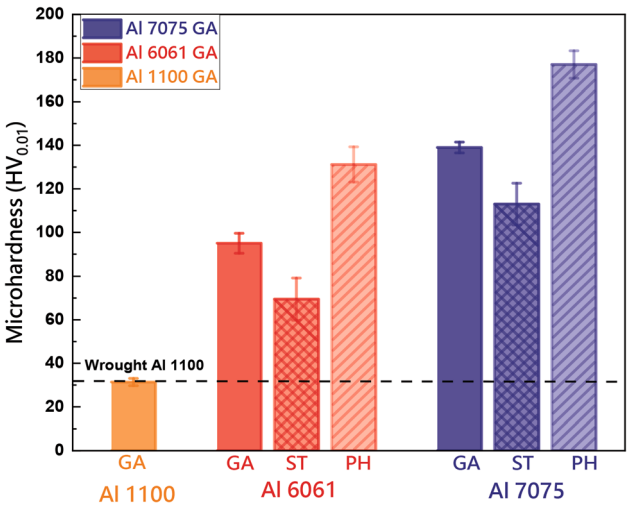

Fig. 6 Microhardness of gas-atomized (GA), solution-treated (ST), and precipitation-hardened (PH) Al 1100, Al 6061, and Al 7075 powders. Precipitation-hardened powder showed the highest average microhardness, followed by gas-atomized and solution-treated powder

69.5 ± 9.70 HV, and the precipitation-hardened one showed a 38% increase to 131.2 ± 8.1 HV. Similarly, the average microhardness of the gas-atomized Al 7075 powder is 139.0 ± 2.5 HV. The corresponding value of solution-treated Al 7075 showed an 18.7% decrease to 113.0 ± 5.6 HV, and precipitation-hardened one showed a 27.4% increase to 177.0 ± 6.3 HV. Compared to the nanoscale response, the standard deviation in microhardness is less. This indicates that the microhardness probed from multiple grains and grain boundaries at a larger length scale exhibits a more homogeneous mechanical response.

In the case of Al 6061 and Al 7075, the average microhardness followed an increasing trend progressively from solution-treated through gas-atomized to precipitation-hardened powder. Multiple grain and grain boundaries simultaneously influence indentation at micrometer length scales. The solution-treated powder contains no precipitates or segregated secondary phases in the microstructure. It only has solid solution strengthening in the Al lattice. Therefore, when a force of 0.098 N is applied, the resistance offered solely by solid solution strengthening is inferior to that provided by secondary phases and precipitates present at the grain boundaries. Therefore, solution-treated powder exhibited the lowest average microhardness in all cases. This trend is in contrast to the trend observed in nanoscale mechanical behavior. In the case of gas-atomized powder, the intermetallic solute atom network segregated at the grain boundary provides the necessary resistance to the force, which is manifested as an enhancement in the average powder microhardness. On the other hand, the precipitation-hardened powder showed the highest average microhardness due to fine precipitates. The

precipitates restrict the motion of dislocations, requiring higher stress for plastic flow that translates to a higher microhardness.

The microscale mechanical behavior of the powder can be correlated with the macroscopic properties of the cold-sprayed coating. From these observations, it can be concluded that precipitation hardening can be employed to develop high-strength Al alloy powder. With the solid-state nature of cold spray deposition, the high strength will be preserved in the final coatings compared to the gas-atomized counterpart.

Elastic Modulus and its Distribution in Gas-Atomized and Heat-treated Al Alloy Powders

The cold spray deposition process relies on the overall deformation of the powder. The extent and variation of deformation in the powder are dependent on the localized elastic modulus and its distribution in the particle. The localized elastic modulus of the powder is measured from the unloading curve of the quasi-static nanoindentation experiments. The distribution of elastic modulus over the powder cross-section is probed at a high resolution by elastic modulus mapping using nano-DMA. Figure 7 depicts the localized average elastic modulus of Al 1100, Al 6061, and Al 7075 powder in the gas-atomized and heat-treated conditions. Gas-atomized Al 1100 showed the lowest average elastic modulus compared to alloyed Al powders, as 60.0 ± 3.2 GPa. In Al 6061 and Al 7075, gas-atomized and solution-treated powder showed similar average elastic modulus around 62.8 ± 3.6 and 65.1 ± 4.4 GPa, respectively. However, the average elastic modulus of the precipitation-hardened Al 6061 and Al 7075 powder showed a 17% and 11% increase to 72.5 ± 3.3 and 73.8 ± 2.8 GPa compared to the gas-atomized powder, respectively. Thus, it can be concluded that the precipitates formed during the precipitation hardening enhance the resistance to elastic deformation manifested as an increase in average elastic modulus. The overall summary of the hardness and elastic modulus of the gas-atomized and heat-treated powders are presented in Table 5.

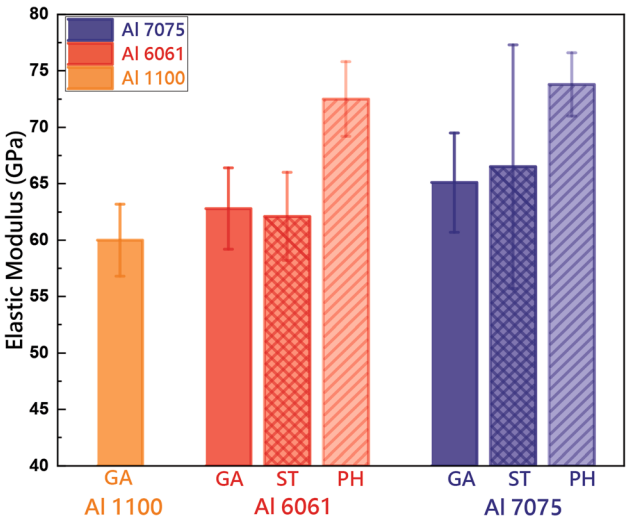

Fig. 7 Average elastic modulus of Al 1100, Al 6061, and Al 7075 powder in the gas-atomized (GA), solution-treated (ST), and precipitation-hardened (PH) conditions. The precipitation-hardened powder showed the highest elastic modulus, whereas solution-treated and gas-atomized powder exhibited a similar elastic modulus response

The modulus maps represent the elastic modulus distribution at a micro-length scale with respect to the variation in microstructural features such as grain interior, grain boundary, nanoscale precipitates, and porosity. Figure 8(a), (b) and (c) and 9(a), (b), (c) and (d) presents the BSE microstructure of the gas-atomized, solution-treated, and precipitation-hardened Al 1100, Al 6061, and Al 7075 powder. The corresponding scanning probe microstructure on an area of 20 × 20 μm^2 is presented in Fig. 8(d), (e) and (f) and 9(e), (f), (g) and (h). The elastic modulus distribution in these sections is depicted in Fig. 8(g), (h) and (i) and 9(i), (j), (k) and (l) as a high-resolution image of 256 × 256 pixels. The elastic modulus distribution is presented as a gradation in color. The elastic modulus value indicated by each color is presented as a scale varying from 0 to 100 GPa in the images. From Fig. 8(g), (h), and (i), it can be observed that the distribution of elastic modulus in the gas-atomized powder is non-uniform across the cross-section. From the earlier discussions, the microstructure of gas-atomized powder is characterized by heterogeneously segregated secondary phases. Hence, the elastic modulus is high in certain pockets, with around 90 to 100 GPa as red. Overall the elastic modulus across the grains ranges from 30 to 100 GPa. Therefore, the distribution of elastic modulus is non-homogeneous.

The elastic modulus distribution of solution-treated and precipitation-hardened Al 6061 and Al 7075 powders is presented in Fig. 9(i), (j), (k) and (l). Compared to the gas-atomized powder (Fig. 8g, h and i), the elastic modulus distribution in the solution-treated and precipitation-hardened powder is uniform. The blue shaded areas representing low elastic modulus regions of value 30 to 40 GPa observed in the gas-atomized powder are no longer discernible in the solution-treated and precipitation-hardened powder. A high modulus region around 90 to 100 GPa in red is visible throughout the powder cross-section in the precipitation-hardened powder. These are the hard intermetallic phases produced during precipitation hardening heat treatment. The observations show that heat treatment is a promising method for altering the microstructure of the gas atomized powder to achieve uniformity and homogeneous distribution of elastic modulus. This uniform

Table 5 Nanohardness, microhardness, and elastic modulus of the gas-atomized, solution-treated, and precipitation-hardened Al alloy powder

Al Powders	Nanohardness (GPa)	Microhardness (GPa)	Elastic Modulus (GPa)
Al 1100-GA	0.72 ± 0.04	0.31 ± 0.01	60.00 ± 3.20
Al 6061-GA	1.00 ± 0.10	0.93 ± 0.05	62.80 ± 3.60
Al 6061-ST	1.30 ± 0.04	0.68 ± 0.10	62.10 ± 3.90
Al 6061-PH	1.60 ± 0.03	1.29 ± 0.08	72.50 ± 3.30
Al 7075-GA	1.50 ± 0.10	1.36 ± 0.02	65.10 ± 4.40
Al 7075-ST	1.70 ± 0.10	1.11 ± 0.09	66.50 ± 10.80
Al 7075-PH	1.80 ± 0.04	1.74 ± 0.06	73.80 ± 2.80

distribution of elastic properties is desirable for manufacturing high-strength Al alloy coatings.

During cold spray deposition, when the powder deforms, the periphery of the powder leads to the formation of the jetting regions, and the interior of the powder forms the core of the splats. The average nano-elastic modulus at the interior of the powder determines the modulus at the interior of the splat and that at the periphery determines the modulus of the jetting regions. The results obtained from this investigation show that cold spraying with gas-atomized powders is expected to yield a deposit with non-uniform stiffness due to differential modulus and recrystallizations at the splat and jetting regions. In contrast, treated and precipitation-hardened powders spraying with the solution will yield homogeneous stiffness deposits across splats. Precipitation-hardened powder is expected to yield a higher average bulk elastic modulus.

Time-Dependent Aging Behavior of Al 6061 and Al 7075 Alloy Powder

The hardness of Al alloys undergoes evolution due to continued precipitate formation occurring at the microscopic level. Therefore, it is crucial to unravel the aging behavior of Al alloy powder. This can be further used to develop customized heat treatment protocols for cold spray deposition. The aging plot of Al 6061 powder solution treated at 545 °C and aged at 160 °C from 0 to 24 h is presented in Fig. 10(a). The lowest average microhardness is obtained at 0 h (Region I), the starting point of the aging curve at 69.50 ± 9.70 HV. From 3 to 18 h (Region II), the hardness progressively increased to a maximum at the 18th hour up to 131.20 ± 8.10 HV. Beyond the 18th hour (Region III), the average microhardness progressively decreased to a minimum at 97.50 ± 11.60 HV. The aging curve of Al 7075 powder solution treated at 505 °C and aged at 130 °C from 0 to 48 h is presented in Fig. 10(b). The lowest average microhardness is obtained at 0 h (Region I), the starting point of the aging curve at 113.00 ± 9.60 HV. From 3 to 24 h (Region II), the hardness progressively increased to a maximum at the 24th hour up to 177.00 ± 6.30 HV. Beyond the 24th hour (Region III), the average microhardness progressively decreased to a minimum at 105.00 ± 19.00 HV. Thus, the critical insight obtained here was that the peak hardness in Al 6061 and Al 7075 was acquired at 18 and 24 h, respectively. Cold spraying could be conducted with powder in this peak-aged condition to preserve the high hardness in the coating. Hence, particularly in Al 7075, the rest of the aging treatments were designed only to capture the decreasing trend while keeping experimental cost and sample screening time minimal and were conducted at larger time intervals of 2 h (Fig. 10b).

The precipitation sequence of Al 6061 (Al-Mg-Si composition), where Mg and Si are the main solute atoms, is supersaturated solid solution (SSSS), coherent G. P zones of solute clusters (Mg and Si), metastable β″ (Mg_2Si), metastable β′ (Mg_2Si), and stable β (Mg_2Si) (Ref 64). The precipitation sequence of Al 7075 (Al-Zn-Mg composition), where Mg and Zn are the main solute atoms, is a supersaturated solid solution (SSSS), coherent GP zones of solute clusters (Mg, Zn), η′ ($MgZn_2$), and stable η ($MgZn_2$) (Ref 65). The crystal structure of Mg_2Si and $MgZn_2$ is face-centered cubic and hexagonal close-packed, respectively (Ref 64, 65). Here, Mg_2Si and $MgZn_2$ are the main strengthening phases of Al 6061 and Al 7075 alloy.

In both Al alloys, the aging curve shows that the average microhardness increases up to a peak value and then decreases. When aging starts, coherent GP zones are formed in the powder. These GP zones will restrict the dislocation motion when a compressive force is applied. However, the dislocations can cut through the GP zones, manifested as the lowest hardness at the initial aging hours. The precipitate size increases with aging time. In these regions, dislocations spend more energy cutting through the precipitate, manifesting as an average microhardness increase. After the peak hardening, the average microhardness decreases in the aging plot due to precipitate coarsening. Consequently, dislocation cannot cut through the precipitates but will bow around the precipitate. Lower stress is required for dislocation bowing, which is observed as a lower hardness value (Ref 66).

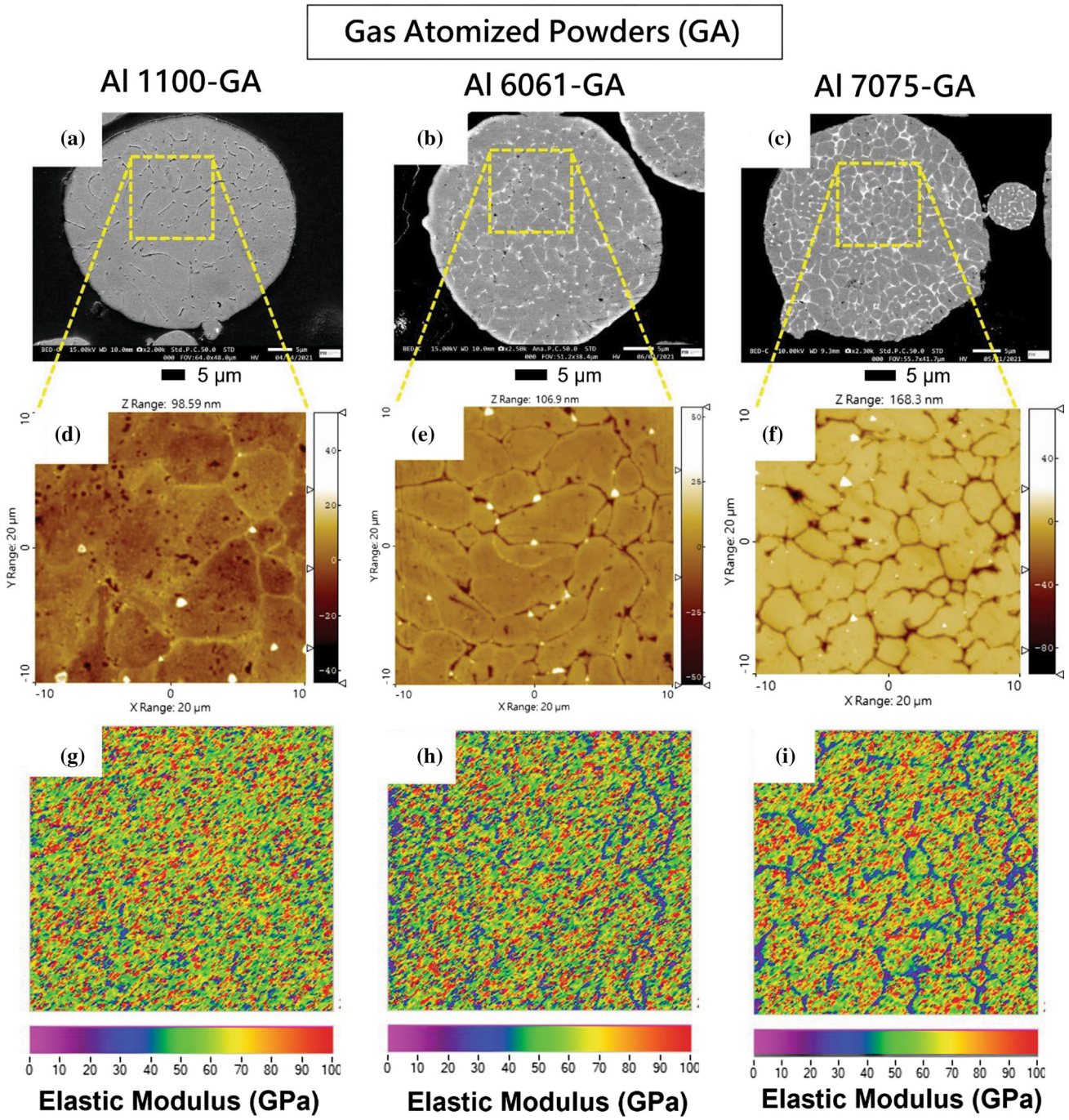

Fig. 8 BSE micrographs of the gas-atomized (GA) Al alloy powder, (a) Al 1100-GA, (b) Al 6061-GA, and (c) Al 7075 GA. The corresponding topographic image obtained by scanning probe microscopy and the distribution of elastic modulus acquired over an area of 20 × 20 µm on (d & g) Al 1100-GA, (e & h) Al 6061-GA (f & i) Al 7075 GA. Elastic modulus distribution is a high-resolution map of 256 × 256 pixels. The gas-atomized powder is characterized by a non-uniform elastic modulus ranging from 30 to 100 GPa

Effect of Aging Behavior on Cold Spray Deposition

The aging behavior of Al 6061 and Al 7075 powders exhibited hardness evolution with time due to the previously discussed precipitation sequence. The variation in hardness affects the manufactured coating's cold spray deposition and hardness. This section discusses the aspects of deposition and post-deposition treatments that must be considered during cold spray of aged Al alloy powder in light of three distinct regions in the aging curve. The three distinct areas in the aging curve are presented in Fig. 10(a) and (b), and the corresponding precipitate growth is illustrated in Fig. 10(c).

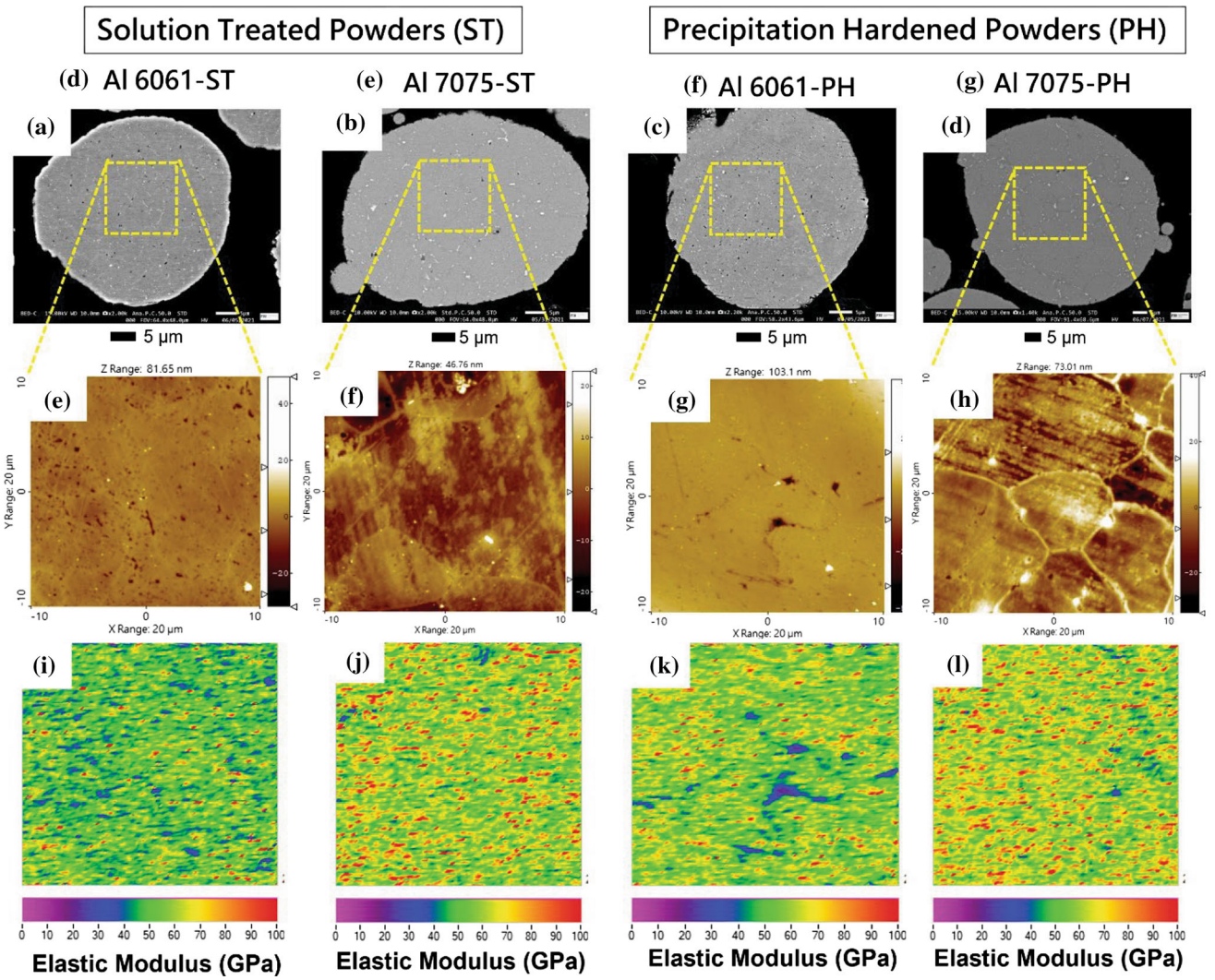

Fig. 9 BSE micrographs of the solution-treated (ST) and precipitation-hardened (PH) Al alloy powder (a) Al 6061-ST, (b) Al 7075-ST, (c) Al 6061-PH (d) Al 7075-PH. The corresponding topography image obtained by scanning probe microscopy and the distribution of elastic modulus acquired over an area of 20 × 20 µm, (e & i) Al 6061-ST, (f & j) Al 7075-ST (g & k) Al 6061-PH (h & l) Al 7075-PH. Elastic modulus distribution is a high-resolution map of 256 × 256 pixels. After heat treatment, the elastic modulus is uniformly distributed in the solution-treated and precipitation-hardened powder

Region I represents the under-aged powders from 0 to 3 h where hardness has not significantly increased. Due to the relatively low hardness of the powder, plastic deformation will be severe during cold spray deposition. Severe plastic deformation of these Al powders can result in cracks in the jetting area of splats, resulting in poor adhesion and mechanical interlocking with the substrate and prior deposited splats (Ref 9). Subsequently, this can result in poor intersplat bonding and extensive splat sliding when external stresses are applied (Ref 9). In addition, due to the relatively low hardness of the powder, the resulting coating will also have poor hardness (Ref 9). However, the Al powders in this region exhibit high deposition efficiency during the cold spray (Ref 16). Hence, for improved performance, cold spray coatings manufactured using powder from Region I should be subjected to post-deposition heat treatments to enhance intersplat bonding and precipitation of hard secondary phases.

Region II is characterized by increasing hardness from 3 to 18 h in Al 6061 and 3 to 24 h in Al 7075 powder to reach peak hardening. The hard powder induces a 'peening' effect during cold spray deposition, improving the intersplat bonding and adhesion to the substrate (Ref 9, 17). The area around intersplat and precipitates will be severely deformed during severe plastic deformation, leading to high dislocation density (Ref 9, 17). The final coating will thus exhibit improved hardness and strength from work or strain hardening (Ref 9, 17). This can be explained by using the Taylor formula as work hardening is directly proportional to the dislocation density (Ref 17),

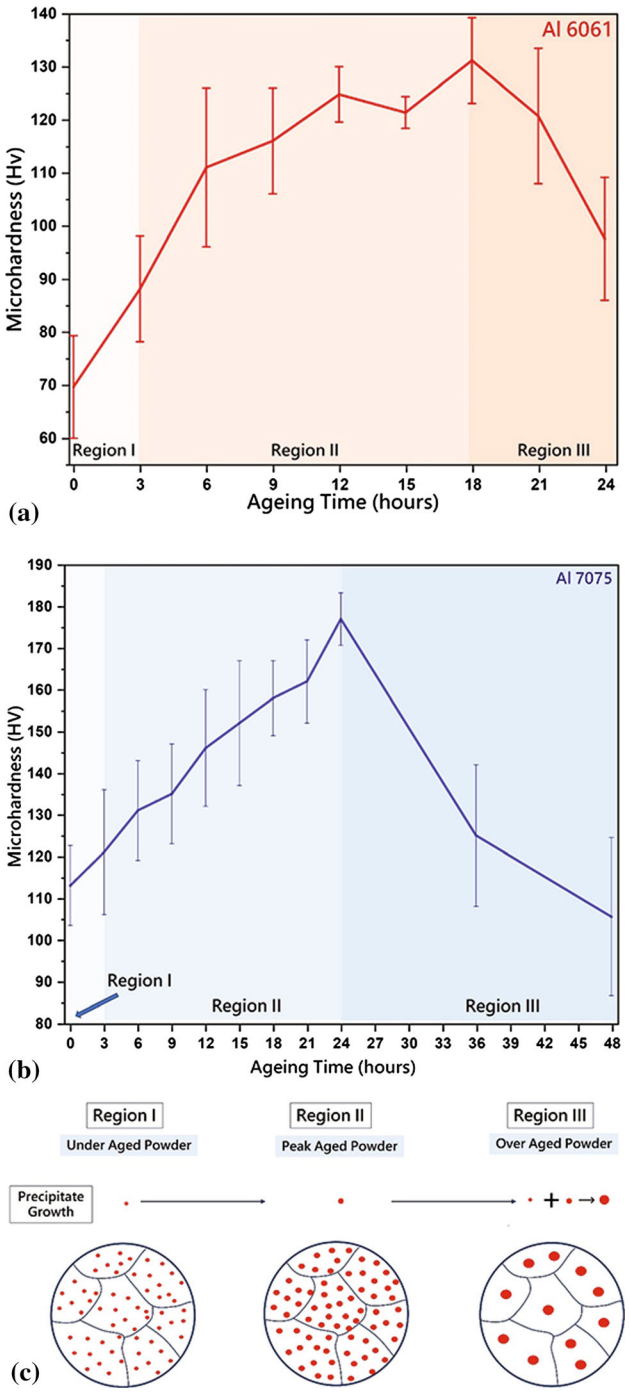

Fig. 10 Evolution of hardness of Al alloy powder with progressive time duration during aging of (a) Al 6061 solution-treated at 545 °C and aged at 160 °C and (b) Al 7075 powder solution treated at 505 °C and aged at 130 °C. The aging plots of the powder indicate three different regions, namely region I, region II, and region III. These regions show the powder's change in precipitate growth and corresponding microhardness. (c) Illustration of precipitate growth and powder conditions in regions I, II, and III

$$\sigma = \alpha M G b \rho^{1/2} \quad \text{(Eq 2)}$$

where σ(MPa) is the work hardening, α is constant, M is the Taylor factor, G (GPa) is the shear modulus, b (nm) is the magnitude of the Burgers vector, and ρ (m^{-2}) is the dislocation density. Similar observations were made in the cold-sprayed Al-Cu coating and age-hardened Al-Mg-Si alloys, where hardness increased due to severe plastic deformation of the precipitation-hardened alloys (Ref 17, 67). Moreover, in Al-Cu cold-sprayed coating, it is observed that hardness and dislocation density directly relate to the precipitate content. Hence, powder from region II is suitable for manufacturing cold spray coatings (Ref 17).

Region III is identified by a hardness decline from the peak value, starting from the 18th hour of aging in Al 6061 and the 24th hour of aging in Al 7075. No study is available that utilizes powder from this region to manufacture cold spray coatings. The microstructure of over-aged powder will contain stable, coherent precipitates, which act as inclusion and could create high dislocation density regions in the final coating after severe plastic deformation. Moreover, the lower hardness of the powder generally results in improved ductility, favoring plastic deformation and achieving moderate strength in the final coating.

Thus, it can be concluded that customized heat treatment protocols can be developed for Al alloy powders to developing cold spray coatings with a varying hardness. Heat treatment temperature and time can be correlated to the required hardness in the initial powder to engineer a similar hardness in the final coating. Cold spray coating made using solution-treated powders in the region I and over-aged powders in region III demonstrate high ductility with a compromise in the mechanical strength. In contrast, region II powders can be used to make high-strength Al-alloy coating with medium ductility.

Cold Spray Process Parameters Optimization as a Function of Aged Powder

The cold spray process involves multiple variables that take time to optimize for developing a high-quality coating. These variables can be grouped into powder feedstock parameters such as powder shape, size, and hardness and gas parameters such as gas type, temperature, and pressure, as presented in Fig. 11. These input parameters should be synchronized to achieve optimum sprayability and high deposition efficiency at a low cost. However, extensive experiments must be conducted to determine the optimized combination of parameters (Ref 68). The present study uses a cold spray process simulation tool, KSS, to develop process maps for heat-treated Al 6061 and 7075 powders (Ref 23-59).

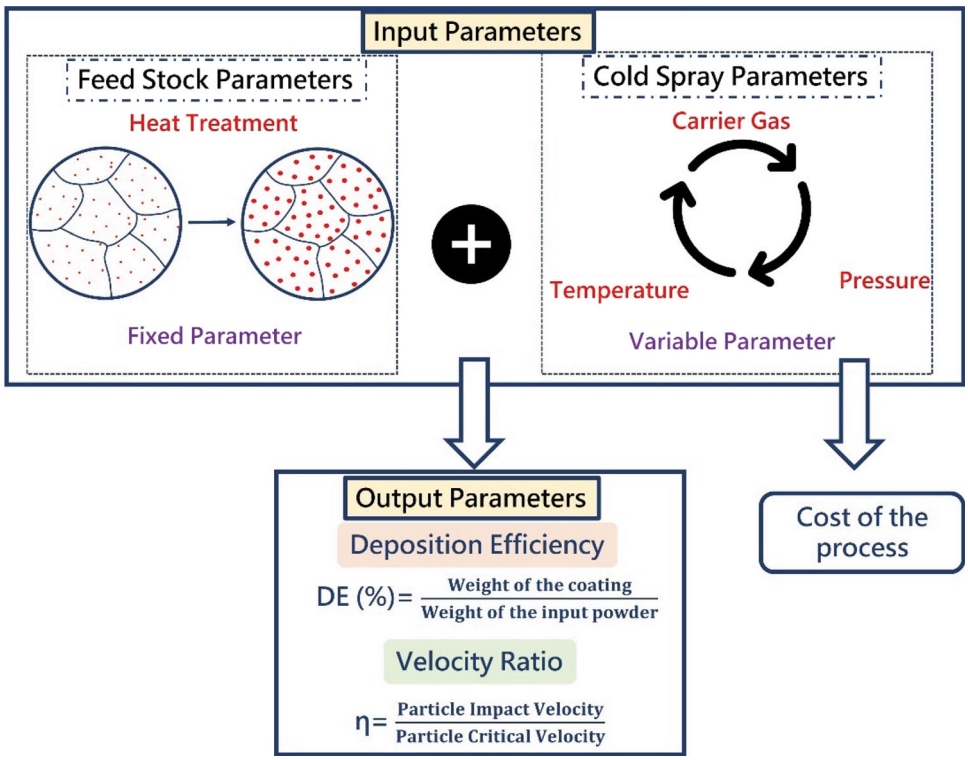

Fig. 11 A framework of correlations between inputs such as powder feedstock and cold spray process parameters with output properties is used for optimization simulations. The processing expense is driven primarily by input parameters such as carrier gas, temperature, and pressure

Table 6 Total particle velocity (V_p) and temperature (T_p) at different aging parameters (AP), process gases, gas temperature (T_g), and gas pressure (P_g).

Gas	T_g (°C)	P_g (bar)	Al 6061			Al 7075		
			AP	V_p(m/s)	T_p(°C)	AP	V_p(m/s)	T_p(°C)
Nitrogen	250	20	545 °C and (0 to 24 h)	504	87	505 °C and (0 to 48 h)	528	72
		40		539	88		558	72
	500	20		601	28		629	224
		40		633	22		661	221
Helium	250	20		1110	21		1196	-11
		40		1229	14		1298	-19
	500	20		1267	143		1378	97
		40		1416	135		1515	86

The particle velocity and particle temperature are the same for each aging temperature and time at the same process temperature and pressure (reported as one value)

(a) Effect of aged powder hardness on particle temperature (T_p), total particle velocity (V_p), and critical velocity (V_c)

During cold spray deposition, the impact particle temperature and the total particle velocity are essential to reach the critical velocity for mechanical interlocking and metallurgical bonding. Table 6 presents the simulated particle velocity and temperature as a function of aged powder hardness from 0 to 48 h at different carrier gases, gas temperature, and gas pressure. The results indicate that the inflight particle velocity and the temperature do not change with aged powder hardness.

In cold spray deposition, powder particles must reach a critical velocity for successful bond formation with the substrate or underlying prior deposited splat. Figure 12 shows the change in critical velocity with aging time for Al 6061 at different process gas, gas temperature, and constant gas pressure. The simulation results show that the critical velocity changes with the evolution of powder hardness at different aging times. At constant process gas parameters,

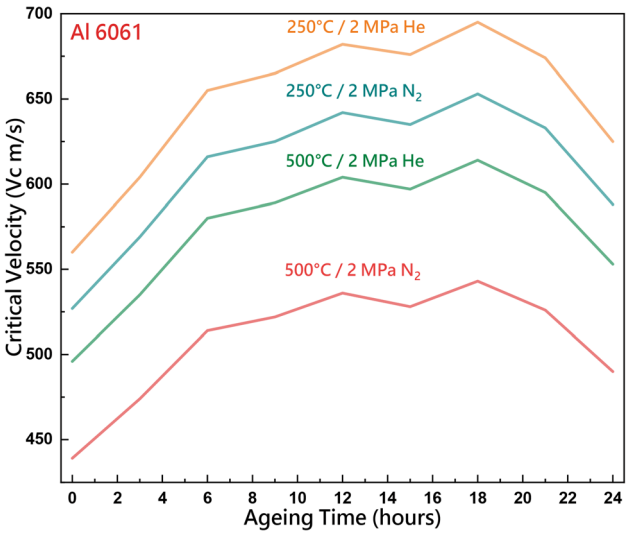

Fig. 12 Variation of critical velocity (Vc) with aging time for Al 6061 powder. The carrier gases used were helium and nitrogen at 250 and 500 °C and the constant pressure of 2 MPa. The critical velocity increases when the hardness of the Al 6061 powder increases at 6, 12, and 18 h. Similarly, the critical velocity decreases when the average hardness of the powder decreases at 15, 21, and 24 h

as the powder hardness increases at 6 h, 12 h, and 18 h, the critical velocity also increases. Similarly, the critical velocity decreases as the powder hardness decreases at 21 and 24 h. The critical velocity is related to inflight particle temperature (Tp, °C), powder properties such as flow stress (σ, MPa), density (ρ, kgcm^{-3}), heat capacity (Cp, JK^{-1}), and melting temperature (Tm, °C), as presented in Eq 3, 4 and 5 (Ref 69).

$$Vc = \sqrt{\frac{a\sigma}{\rho} + bCp(Tm - Tp)} \quad \text{(Eq 3)}$$

$$\sigma = \sigma_{UTS}(1 - \theta) \quad \text{(Eq 4)}$$

$$\theta = \frac{(T - Tref)}{(Tm - Tref)} \quad \text{(Eq 5)}$$

where σ_{UTS} is the ultimate tensile strength of the powder (MPa), T_{ref} is the room temperature (°C). From the above mathematical relations, Eq 3, 4 and 5, the critical velocity directly depends on the ultimate tensile strength of the powder. Thus, the change in aged powder hardness changes the ultimate tensile strength of the powder and hence the critical velocity. Figure 12 also indicates that the critical velocity reduces when gas temperature increases at the same gas type. As the gas temperature increases, the particle velocity, and temperature increase, reducing the critical velocity (Table 6). Hence, even though aging changes the hardness of the powder, optimum selection of process gas and gas temperature is essential for cold spray deposition of Al alloy powders.

(b) Effect of aged powder hardness on velocity ratio and deposition efficiency

The velocity ratio is a significant parameter in cold spray used to produce optimum process maps. The velocity ratio (coating quality factor) represents the sprayability of the aged powder and can be related in terms of particle impact velocity and critical velocity ratio (η) as

$$\eta = \frac{v_p}{v_c} \quad \text{(Eq 6)}$$

The optimum velocity ratio helps in stable coating adhesion and buildup. From section (a), we understood that critical velocity would change with a change in hardness and hence the velocity ratio. As the velocity ratio changes, the deposition efficiency also changes during cold spray deposition. Therefore, the gas temperature is varied from 100 and 600 °C for air, nitrogen, and helium at a constant pressure of 2 MPa to vary the velocity ratio and deposition efficiency to develop a deposition window for aged Al alloy powders. Figure 13(a) and (b) presents the process map of aged Al 6061 and Al 7075 powder that correlates the aging hours with velocity parameter (η) and deposition efficiency. The temperatures from 100 to 400 °C and 100 to 300 °C are reported as the low-temperature regime for air/nitrogen and helium gas, respectively. The corresponding high-temperature regime for air/nitrogen and helium is 500 to 600 °C and 300 to 600 °C, respectively.

The change in velocity ratio manifests as the corresponding change in deposition efficiency in cold spray deposition. The process maps of aged Al 6061 and Al 7075 can be divided into three regions according to the value of the velocity ratio. When the velocity ratio is less than 1 ($\eta < 1$), the particle velocity is less than the critical velocity. This region is characterized by poor substrate adhesion, resulting in poor coating buildup and low deposition efficiency (Ref 69). From Fig. 13(a) and (b), air and nitrogen gas at 100 to 400 °C result in a velocity ratio of less than 1. Due to the low sonic speed of the air and nitrogen gas, the particle velocity at these temperatures is less than the critical velocity for bond initiation. When the velocity ratio is between 1 and 2, the particle velocity is equal to or greater than the critical velocity. Therefore, the total particle velocity results in the powder's bond initiation and thermal softening (Ref 69). From Fig. 13(a) and (b), air and nitrogen gas with a temperature of 500 to 600 °C and helium gas with a temperature of 100 to 300 °C result in a velocity ratio between 1 and 2. This region is characterized by good coating buildup and high deposition efficiency for depositing aged Al alloy powders. When the velocity ratio is above 2, the powder particle velocity is too high for critical velocity. This can result in hydrodynamic substrate erosion by the powder particle resulting in poor or

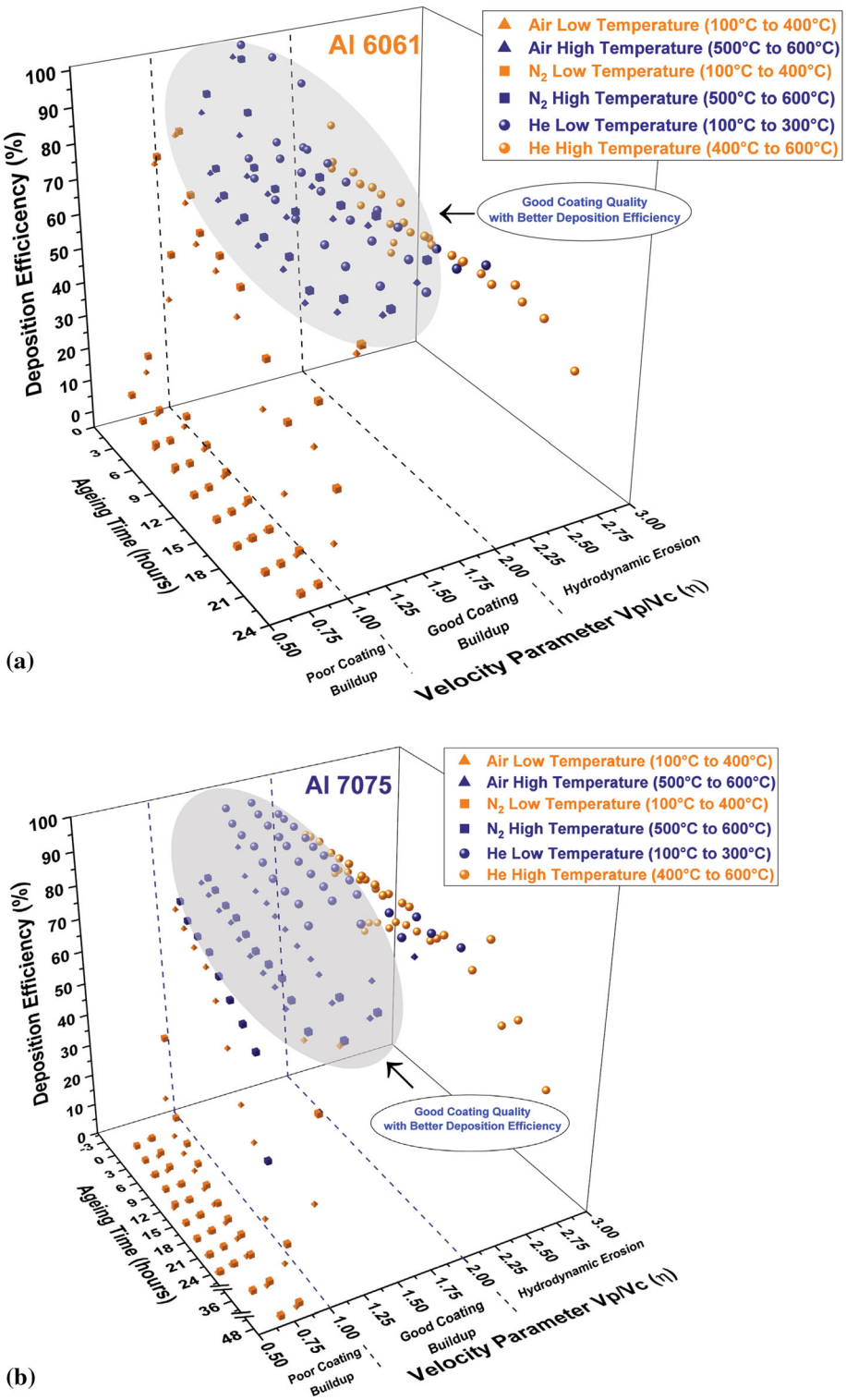

Fig. 13 Cold spray process map developed for aged Al alloy powder, showing the effect of aging treatment on velocity parameter and deposition efficiency in (a) Al 6061 and (b) Al 7075. The gas temperature is varied from 100 to 600 °C at a pressure of 2 MPa for air, nitrogen, and helium. The ellipse in blue color indicates the area of highest deposition efficiency with good coating quality

non-uniform coating buildup (Ref 69). From the process maps, helium gas at temperatures 400 to 600 °C results in a velocity ratio above 2. At these temperatures, the particle velocity is high due to the high sonic speed of helium. Therefore, when the velocity ratio is between 1 and 2, coating buildup and successive improvement in deposition efficiency are observed. The corresponding range of particle velocity and the critical velocity for Al 6061 and 7075 in air, nitrogen, and helium that results in η between 1 and 2 is presented in Table 7.

To recapitulate, the aging of the Al alloy powders changes the microhardness of the powder and, thereby,

Table 7 Range of critical velocity (V_c) and total particle velocity (V_p) at the optimum process parameter window of velocity ratio η between 1 and 2

Heat-treated powder	Carrier gas	Critical velocity (V_c, ms^{-1})	Total particle velocity (V_p, ms^{-1})
Al 6061 Powder	Air (500 to 600 °C)	400 to 550	580 to 623
	Nitrogen (500 to 600 °C)	400 to 536	601 to 635
	Helium (100 to 300 °C)	548 to 740	998 to 1145
Al 7075 Powder	Air (500 to 600 °C)	425 to 594	618 to 652
	Nitrogen (500 to 600 °C)	415 to 584	629 to 663
	Helium (100 to 300 °C)	646 to 858	1056 to 1237

their plastic deformation behavior. The simulation shows that a suitable selection of carrier gas, gas pressure, and temperature will help achieve high deposition efficiencies with the Al powders aged from 0 to 48 h. Air and nitrogen gas with a temperature of 500 to 600 °C and helium gas with a temperature of 100 to 300 °C are the optimum process gas parameters for depositing aged Al 6061 and Al 7075 powder. At these parameters, the deposition efficiency for coating from aged Al alloy powders is between 75 and 98%, irrespective of Al alloy composition, aging temperature, and time.

Conclusions

For the first time, the present investigation establishes comprehensive powder heat treatment protocols for manufacturing high-strength Al alloy powders for cold spray deposition of high-strength coatings. Correlations between heat treatment protocols, microstructural evolutions, and their corresponding role in mechanical responses of powder at the nano- to micrometer length scales are enumerated. The main conclusions derived from this study are.

1. Gas-atomized Al 6061 and Al 7075 powders constitute a non-homogeneous microstructure with Mg-, Si-, Zn-, and Fe-rich solute atoms or secondary phases segregated primarily at the grain boundaries. Heat treatments tailor non-homogeneous microstructures, adapting them for cold spray deposition. Solution treatment above the solvus temperature of the Al alloys dissolves these undesired phases in the Al lattice. In contrast, hardening below the solvus temperature enables controlled precipitation of hard intermetallic phases, primarily Mg_2Si and $MgZn_2$ in Al 6061 and Al 7075 powders, respectively.
2. Nanohardness of 1.6 and 1.8 GPa was achieved in precipitation-hardened Al 6061 and Al 7075 powders, respectively, improving 60 and 20% above their gas-atomized counterparts. This trend of nanohardness is directly translated to the cumulative grains of the powder that exhibit microhardness of 131.2 and 177.0 HV, respectively, enhancements of 38 and 27% compared to that in pristine gas-atomized conditions. Similarly, elastic modulus at the individual grains was enhanced by 17 and 11% in Al 6061 and Al 7075, while at the particle length scale, its distribution was homogenized to a more uniform one.
3. Prolonged aging treatments up to 24 and 48 h in Al 6061 and Al 7075 exhibit 3 distinct regions of hardening due to transitions of mechanism from precipitate cutting to dislocation bowing. Powder heat-treated in regions I and III are expected to generate cold-sprayed coatings with relatively higher ductility compromise mechanical strength. In contrast, those in region II are suitable for high-strength coatings with medium ductility.
4. Experimental powder hardness coupled with cold spray simulation enabled the development of *process maps* that predicted velocity parameters in the sweet spot regime of coating buildup with helium at 100-300 °C and air and nitrogen at 300-500 °C. High deposition efficiencies of 70-98% could be achieved in this regime due to particle adherence, while outside, particle rebound and hydrodynamic erosion mechanisms dominate.

Supplementary Information The online version contains supplementary material available at https://doi.org/10.1007/s11666-022-01455-4.

Acknowledgments The authors acknowledge the financial support of DEVCOM—Army Research Laboratory (ARL) grant W911NF2020256. The Advanced Materials Engineering Research Institute (AMERI) at FIU is greatly acknowledged for all the characterization facilities used in this study.

References

1. Victor Kenneth Champagne and Ozan Cagatay Ozdemir Aaron. Nardi, *Practical Cold Spray*, Springer, Cham, 2021.

2. T.H.V. Steenkiste, J.R. Smith and R.E. Teets, Aluminum Coatings via Kinetic Spray with Relatively Large Powder Particles, *Surf. Coat. Technol.*, 2002, **154**(2-3), p 237-252.
3. R.N. Raoelison, Analytical Description of Solid Particles Kinematics Due to a Fluid Flow and Application to the Depiction of Characteristic Kinematics in Cold Spraying, *Powder Technol.*, 2017, **319**, p 191-203. https://doi.org/10.1016/j.powtec.2017.06.029
4. He. Shiwen, L. Yong and G. Sheng, Cooling Rate Calculation of Non-Equilibrium Aluminum Alloy Powders Prepared by Gas Atomization, *Rare Met. Mater. Eng.*, 2009, **38**(S1), p 353-356.
5. G. von Bradsky and R.A. Ricks, Solidification Microstructures in Rapidly Solidified, Gas Atomized Aluminium-Lithium Alloy Powders, *J. Mater. Sci.*, 1987, **22**(4), p 1469-1476.
6. S. Hariprasad, S.M.L. Sastry and S. Louis, Undercooling and Supersaturation of Alloying Elements in Rapidly Solidified AI-8.5% Fe-1.2% V-1.7% Si Alloy, *J. Mater. Sci.*, 1996, **31**(4), p 921-925. https://doi.org/10.1007/BF00352891.
7. M.R. Rokni, C.A. Widener and V.R. Champagne, Microstructural Evolution of 6061 Aluminum Gas-Atomized Powder and High-Pressure Cold-Sprayed Deposition, *J. Therm. Spray Technol.*, 2014, **23**(3), p 514-524.
8. C. Walde, K. Tsaknopoulos, V. Champagne and D. Cote, Phase Transformations in Thermally Treated Gas-Atomized Al 7075 Powder, *Metallogr. Microstruct. Anal.*, 2020, **9**(3), p 419-427. https://doi.org/10.1007/s13632-020-00641-6
9. A. Sabard, P. McNutt, H. Begg and T. Hussain, Cold Spray Deposition of Solution Heat Treated, Artificially Aged and Naturally Aged Al 7075 Powder, *Surf. Coatings Technol.*, 2020, **385**, p 125367. https://doi.org/10.1016/j.surfcoat.2020.125367
10. L.E. Randaccio, Pre-Heat Treatment of Gas Atomized Al 2024 Powder and Its Effects on the Properties of Cold Spray Coatings, Mater of Science Thesis, Northeastern University, December (2019)
11. K. Tsaknopoulos, J. Grubbs, M. Siopis, A. Nardi and D. Cote, Microstructure and Mechanical Property Evaluation of Aluminum F357 Powder for Cold Spray Applications, *J. Therm. Spray Technol.*, 2021, **30**(3), p 643-654. https://doi.org/10.1007/s11666-020-01140-4
12. M.R. Rokni, A.T. Nardi, V.K. Champagne and S.R. Nutt, Effects of Preprocessing on Multi-Direction Properties of Aluminum Alloy Cold-Spray Deposits, *J. Therm. Spray Technol.*, 2018, **27**(5), p 818-826. https://doi.org/10.1007/s11666-018-0723-1
13. S. Vijayan, B.A. Bedard, M.A. Gleason, H.R. Leonard, D.L. Cote and M. Aindow, Studies of Thermally Activated Processes in Gas-Atomized Al Alloy Powders: In Situ STEM Heating Experiments on FIB-Cut Cross Sections, *J. Mater. Sci.*, 2019, **54**(13), p 9921-9932. https://doi.org/10.1007/s10853-019-03562-0
14. K. Tsaknopoulos, C. Walde, D. Tsaknopoulos, V. Champagne and D. Cote, Characterization of Thermally Treated Gas-Atomized Al 5056 Powder, *Materials (Basel)*, 2020, **13**(18), p 1-11.
15. A. Sabard, H.L. de Villiers Lovelock and T. Hussain, Microstructural Evolution in Solution Heat Treatment of Gas-Atomized Al Alloy (7075) Powder for Cold Spray, *J. Therm. Spray Technol.*, 2018, **27**(1-2), p 145-158.
16. W.A. Story and L.N. Brewer, Heat Treatment of Gas-Atomized Powders for Cold Spray Deposition, *Metall. Mater. Trans. A Phys. Metall. Mater. Sci.*, 2018, **49**(2), p 446-449. https://doi.org/10.1007/s11661-017-4428-8
17. T. Liu, J.D. Leazer, S.K. Menon and L.N. Brewer, Microstructural Analysis of Gas Atomized Al-Cu Alloy Feedstock Powders for Cold Spray Deposition, *Surf. Coatings Technol.*, 2018, **350**, p 621-632. https://doi.org/10.1016/j.surfcoat.2018.07.006
18. A. Sabard and T. Hussain, Inter-Particle Bonding in Cold Spray Deposition of a Gas-Atomised and a Solution Heat-Treated Al 6061 Powder, *J. Mater. Sci.*, 2019, **54**(18), p 12061-12078.
19. C. Walde, D. Cote, V. Champagne and R. Sisson, Characterizing the Effect of Thermal Processing on Feedstock Al Alloy Powder for Additive Manufacturing Applications, *J. Mater. Eng. Perform.*, 2019, **28**(2), p 601-610. https://doi.org/10.1007/s11665-018-3550-0
20. B.A. Bedard, T.J. Flanagan, A.T. Ernst, A. Nardi, A.M. Dongare, H.D. Brody, V.K. Champagne, S.W. Lee and M. Aindow, Microstructure and Micromechanical Response in Gas-Atomized Al 6061 Alloy Powder and Cold-Sprayed Splats, *J. Therm. Spray Technol.*, 2018, **27**(8), p 1563-1578. https://doi.org/10.1007/s11666-018-0785-0
21. A.T. Ernst, P. Kerns, A. Nardi, H.D. Brody, A.M. Dongare, S.W. Lee, V.K. Champagne, S.L. Suib and M. Aindow, Surface States of Gas-Atomized Al 6061 Powders-Effects of Heat Treatment, *Appl. Surf. Sci.*, 2020, **534**, p 147643.
22. K. Tsaknopoulos, C. Walde, V. Champagne and D. Cote, Gas-Atomized Al 6061 Powder: Phase Identification and Evolution During Thermal Treatment, *Jom*, 2019, **71**(1), p 435-443. https://doi.org/10.1007/s11837-018-3175-7
23. A. List, F. Gärtner, T. Mori, M. Schulze, H. Assadi, S. Kuroda and T. Klassen, Cold Spraying of Amorphous Cu50Zr50 Alloys, *J. Therm. Spray Technol.*, 2014, **24**(1-2), p 108-118.
24. T. Schmidt, H. Assadi, F. Gärtner, H. Richter, T. Stoltenhoff, H. Kreye and T. Klassen, Erratum: From Particle Acceleration to Impact and Bonding in Cold Spraying, *J. Therm. Spray Technol.*, 2009, **18**(5-6), p 1038. https://doi.org/10.1007/S11666-009-9357-7
25. T. Schmidt, H. Assadi, F. Gärtner, H. Richter, T. Stoltenhoff, H. Kreye and T. Klassen, From Particle Acceleration to Impact and Bonding in Cold Spraying, *J. Therm. Spray Technol.*, 2009, **18**(5-6), p 794-808.
26. H. Assadi, T. Schmidt, H. Richter, J.O. Kliemann, K. Binder, F. Gärtner, T. Klassen and H. Kreye, On Parameter Selection in Cold Spraying, *J. Therm. Spray Technol.*, 2011, **20**(6), p 1161-1176.
27. J. Cizek, M. Vilemova, F. Lukac, M. Koller, J. Kondas and R. Singh, Cold Sprayed Tungsten Armor for Tokamak First Wall, *Coatings*, 2019, **9**(12), p 1-15.
28. S. Krebs, F. Gärtner and T. Klassen, Cold Spraying of Cu-Al-Bronze for Cavitation Protection in Marine Environments, *J. Therm. Spray Technol.*, 2014, **24**(1-2), p 126-135.
29. W. Sun, A.W.Y. Tan, A. Bhowmik, I. Marinescu, X. Song, W. Zhai, F. Li and E. Liu, Deposition Characteristics of Cold Sprayed Inconel 718 Particles on Inconel 718 Substrates with Different Surface Conditions, *Mater. Sci. Eng. A*, 2018, **720**, p 75-84. https://doi.org/10.1016/j.msea.2018.02.059
30. G. Mauer, R. Singh, K.H. Rauwald, S. Schrüfer, S. Wilson and R. Vaßen, Diagnostics of Cold-Sprayed Particle Velocities Approaching Critical Deposition Conditions, *J. Therm. Spray Technol.*, 2017, **26**(7), p 1423-1433.
31. P. Coddet, C. Verdy, C. Coddet and F. Debray, Effect of Cold Work, Second Phase Precipitation and Heat Treatments on the Mechanical Properties of Copper-Silver Alloys Manufactured by Cold Spray, *Mater. Sci. Eng. A*, 2015, **637**, p 40-47. https://doi.org/10.1016/j.msea.2015.04.008
32. R.G. Neo, K. Wu, S.C. Tan and W. Zhou, Effect of Spray Distance and Powder Feed Rate on Particle Velocity in Cold Spray Processes, *Metals (Basel)*, 2022, **12**(1), p 1-15.
33. A. Ardeshiri Lordejani, L. Vitali, M. Guagliano and S. Bagherifard, Estimating Deposition Efficiency and Chemical Composition Variation along Thickness for Cold Spraying of Composite Feedstocks, *Surf. Coatings Technol.*, 2022, **436**, p 128239. https://doi.org/10.1016/j.surfcoat.2022.128239

34. O. Stier, Fundamental Cost Analysis of Cold Spray, *J. Therm. Spray Technol.*, 2014, **23**(1-2), p 131-139.
35. M. Flores, Optimization of Cold-Sprayed Nickel Alloy 625 Thick Deposits by Cold Spray Using the KSS Software, *IMedPub J.*, 2022, **8**(2).
36. W. Sun, A. Bhowmik, A.W.Y. Tan, R. Li, F. Xue, I. Marinescu and E. Liu, Improving Microstructural and Mechanical Characteristics of Cold-Sprayed Inconel 718 Deposits via Local Induction Heat Treatment, *J. Alloys Compd.*, 2019, **797**, p 1268-1279. https://doi.org/10.1016/j.jallcom.2019.05.099
37. R. Singh, S. Schruefer, S. Wilson, J. Gibmeier and R. Vassen, Influence of Coating Thickness on Residual Stress and Adhesion-Strength of Cold-Sprayed Inconel 718 Coatings, *Surf. Coatings Technol.*, 2018, **350**, p 64-73. https://doi.org/10.1016/j.surfcoat.2018.06.080
38. A. Elsenberg, M. Busato, F. Gärtner, A. List, A. Bruera, G. Bolelli, L. Lusvarghi and T. Klassen, Influence of MAX-Phase Deformability on Coating Formation by Cold Spraying, *J. Therm. Spray Technol.*, 2021, **30**(3), p 617-642.
39. A.W.Y. Tan, J.Y. Lek, W. Sun, A. Bhowmik, I. Marinescu, X. Song, W. Zhai, F. Li, Z. Dong, C.B. Boothroyd and E. Liu, Influence of Particle Velocity When Propelled Using N2 or N2-He Mixed Gas on the Properties of Cold-Sprayed Ti6Al4V Coatings, *Coatings*, 2018, **8**(9), p 327.
40. N. Cinca, A. List, F. Gärtner, J.M. Guilemany and T. Klassen, Influence of Spraying Parameters on Cold Gas Spraying of Iron Aluminide Intermetallics, *Surf. Coatings Technol.*, 2015, **268**, p 99-107. https://doi.org/10.1016/j.surfcoat.2014.07.070
41. Z. Arabgol, M. Villa Vidaller, H. Assadi, F. Gärtner and T. Klassen, Influence of Thermal Properties and Temperature of Substrate on the Quality of Cold-Sprayed Deposits, *Acta Mater. Acta Materialia Inc.*, 2017, **127**, p 287-301. https://doi.org/10.1016/j.actamat.2017.01.040
42. H. Che, P. Vo and S. Yue, Investigation of Cold Spray on Polymers by Single Particle Impact Experiments, *J. Therm. Spray Technol.*, 2019, **28**(1-2), p 135-143. https://doi.org/10.1007/s11666-018-0801-4
43. H. Che, S. Yue, and P. Vo, Investigation of Cold Spray on Polymers by Single Particle Impact Experiments, Proc. Int. Therm. Spray Conf., 173-178. May 2018
44. P. Coddet, C. Verdy, C. Coddet and F. Debray, Mechanical Properties of Cu-0.1Ag Alloys Deposited by Cold Spray with Various Powder Feed Rate and Heat Treatment, *J. Therm. Spray Technol.*, 2014, **24**(1-2), p 119-125.
45. H. Che, X. Chu, P. Vo and S. Yue, Metallization of Various Polymers by Cold Spray, *J. Therm. Spray Technol.*, 2018, **27**(1-2), p 169-178.
46. A.W.Y. Tan, J.Y. Lek, W. Sun, A. Bhowmik, I. Marinescu, P.J. Buenconsejo, Z. Dong and E. Liu, Microstructure, Mechanical and Tribological Properties of Cold Sprayed Ti6Al4V-CoCr Composite Coatings, *Compos. Part B Eng.*, 2020, **202**, p 108280. https://doi.org/10.1016/j.compositesb.2020.108280
47. P. Coddet, C. Verdy, C. Coddet and F. Debray, On the Mechanical and Electrical Properties of Copper-Silver and Copper-Silver-Zirconium Alloys Deposits Manufactured by Cold Spray, *Mater. Sci. Eng. A*, 2016, **662**, p 72-79. https://doi.org/10.1016/j.msea.2016.03.049
48. L.I. Pérez-Andrade, F. Gärtner, M. Villa-Vidaller, T. Klassen, J. Muñoz-Saldaña and J.M. Alvarado-Orozco, Optimization of Inconel 718 Thick Deposits by Cold Spray Processing and Annealing, *Surf. Coatings Technol.*, 2019, **378**, p 124997. https://doi.org/10.1016/j.surfcoat.2019.124997
49. M. Hauer, F. Gärtner, S. Krebs, T. Klassen, M. Watanabe, S. Kuroda, W. Krömmer and K.M. Henkel, Process Selection for the Fabrication of Cavitation Erosion-Resistant Bronze Coatings by Thermal and Kinetic Spraying in Maritime Applications, *J. Therm. Spray Technol.*, 2021, **30**(5), p 1310-1328.
50. C. Huang, M. Arseenko, L. Zhao, Y. Xie, A. Elsenberg, W. Li, F. Gärtner, A. Simar and T. Klassen, Property Prediction and Crack Growth Behavior in Cold Sprayed Cu Deposits, *Mater. Des.*, 2021, **206**, p 109826. https://doi.org/10.1016/j.matdes.2021.109826
51. M.V. Vidaller, A. List, F. Gaertner, T. Klassen, S. Dosta and J.M. Guilemany, Single Impact Bonding of Cold Sprayed Ti-6Al-4V Powders on Different Substrates, *J. Therm. Spray Technol.*, 2015, **24**(4), p 644-658.
52. S. Bagherifard, J. Kondas, S. Monti, J. Cizek, F. Perego, O. Kovarik, F. Lukac, F. Gaertner and M. Guagliano, Tailoring Cold Spray Additive Manufacturing of Steel 316 L for Static and Cyclic Load-Bearing Applications, *Mater. Des.*, 2021, **203**, p 109575. https://doi.org/10.1016/j.matdes.2021.109575
53. C. Huang, A. List, J. Shen, B. Fu, S. Yin, T. Chen, B. Klusemann, F. Gärtner and T. Klassen, Tailoring Powder Strengths for Enhanced Quality of Cold Sprayed Al6061 Deposits, *Mater. Des.*, 2022, **215**, p 110494. https://doi.org/10.1016/j.matdes.2022.110494
54. N. Fan, J. Cizek, C. Huang, X. Xie, Z. Chlup, R. Jenkins, R. Lupoi and S. Yin, A New Strategy for Strengthening Additively Manufactured Cold Spray Deposits through In-Process Densification, *Addit. Manuf.*, 2020, **36**, p 101626. https://doi.org/10.1016/j.addma.2020.101626
55. M. Terrone, A. Ardeshiri Lordejani, J. Kondas and S. Bagherifard, A Numerical Approach to Design and Develop Freestanding Porous Structures through Cold Spray Multi-Material Deposition, *Surf. Coatings Technol.*, 2021, **421**, p 127423. https://doi.org/10.1016/j.surfcoat.2021.127423
56. K. Wu, W. Sun, A.W.Y. Tan, I. Marinescu, E. Liu and W. Zhou, An Investigation into Microstructure, Tribological and Mechanical Properties of Cold Sprayed Inconel 625 Coatings, *Surf. Coatings Technol.*, 2021, **424**, p 127660. https://doi.org/10.1016/j.surfcoat.2021.127660
57. G. Mauer, K.H. Rauwald, Y.J. Sohn and T.E. Weirich, Cold Gas Spraying of Nickel-Titanium Coatings for Protection Against Cavitation, *J. Therm. Spray Technol.*, 2021, **30**(1-2), p 131-144. https://doi.org/10.1007/s11666-020-01139-x
58. T. Lindner, M. Löbel, M. Grimm and J. Fiebig, Cold Gas Spraying of Solution-Hardened 316L Grade Stainless Steel Powder, *Metals (Basel)*, 2022, **12**(1), p 1-11.
59. C. Huang, A. List, F. Gartner and T. Klassen, Cold Spray Deposition of Functionally Graded Al-SiC Composites, Available at SSRN: https://ssrn.com/abstract=4097864 or https://doi.org/10.2139/ssrn.4097864.
60. B.C. Sousa, M.A. Gleason, B. Haddad, V.K. Champagne, A.T. Nardi and D.L. Cote, Nanomechanical Characterization for Cold Spray: From Feedstock to Consolidated Material Properties, *Metals (Basel)*, 2020, **10**(9), p 1-71.
61. J. Beddoes, Design of Solution Heat Treatments for Aerospace Alloys, *Can. Metall. Q.*, 2011, **50**(3), p 215-221.
62. C.W. Lin, F.Y. Hung and T.S. Lui, Microstructure Evolution and Microstructural Characteristics of Al-Mg-Si Aluminum Alloys Fabricated by a Modified Strain-Induced Melting Activation Process, *Metals (Basel)*, 2018, **8**(1), p 3.
63. X. Zhang and T. Chen, Solution Treatment Behaviors of 6061 Aluminum Alloy Prepared by Powder Thixoforming, *Mater. Res.*, 2018, **21**(4), p e20180057. https://doi.org/10.1590/1980-5373-mr-2018-0057.
64. T. Maeda, K. Kaneko, T. Namba, Y. Koshino, Y. Sato, R. Teranishi and Y. Aruga, Structural and Compositional Study of Precipitates in Under-Aged Cu-Added Al-Mg-Si Alloy, *Sci. Rep.*, 2018, **8**(1), p 1-5. https://doi.org/10.1038/s41598-018-35134-8

65. D.I. Richard and P.N. Adler, Calorimetric Studies of 7000 Series Aluminum Alloys: I. Matrix Precipitate Characterization of 7075, *Metall. Trans. A*, 1977, **8**(7), p 1177-1183.
66. T.R. Prabhu, Effects of Ageing Time on the Mechanical and Conductivity Properties for Various Round Bar Diameters of AA 2219 Al Alloy, *Eng. Sci. Technol. an Int. J.*, 2017, **20**(1), p 133-142. https://doi.org/10.1016/j.jestch.2016.06.003
67. M.H. Farshidi, M. Kazeminezhad and H. Miyamoto, Severe Plastic Deformation of 6061 Aluminum Alloy Tube with Pre and Post Heat Treatments, *Mater. Sci. Eng. A*, 2013, **563**, p 60-67. https://doi.org/10.1016/j.msea.2012.11.025
68. A.K. Keshri, R. Patel and A. Agarwal, Comprehensive Process Maps to Synthesize High Density Plasma Sprayed Aluminum Oxide Composite Coatings with Varying Carbon Nanotube Content, *Surf. Coatings Technol.*, 2010, **205**(3), p 690-702. https://doi.org/10.1016/j.surfcoat.2010.07.007
69. H. Assadi, H. Kreye, F. Gärtner and T. Klassen, Cold Spraying–A Materials Perspective, *Acta Mater.*, 2016, **116**, p 382-407. https://doi.org/10.1016/j.actamat.2016.06.034